UC San Diego

UC San Diego Previously Published Works

Title

Polyglutamine-expanded androgen receptor interferes with TFEB to elicit autophagy defects in SBMA.

Permalink

https://escholarship.org/uc/item/8v83h75n

Journal

Nature neuroscience, 17(9)

ISSN

1097-6256

Authors

Cortes, Constanza J
Miranda, Helen C
Frankowski, Harald
et al.

Publication Date

2014-09-01

DOI

10.1038/nn.3787

Peer reviewed

eScholarship.org Powered by the California Digital Library
University of California

Author Manuscript

Author Manuscript

Author Manuscript

Author Manuscript

HHS Public Access

Author manuscript

Nat Neurosci. Author manuscript; available in PMC 2015 March 01.

Published in final edited form as:

Nat Neurosci. 2014 September ; 17(9): 1180–1189. doi:10.1038/nn.3787.

Polyglutamine-expanded androgen receptor interferes with TFEB to elicit pathological autophagy defects in SBMA

Constanza J. Cortes[1,*], **Helen C. Miranda**[1,2,*], **Harald Frankowski**[1], **Yakup Batlevi**[1], **Jessica E. Young**[2], **Amy Le**[1], **Nishi Ivanov**[3], **Bryce L. Sopher**[4], **Cassiano Carromeu**[1], **Alysson R. Muotri**[1,2,5,7,8,9], **Gwenn A. Garden**[4], and **Albert R. La Spada**[1,2,5,6,7,8,9]

[1]Department of Pediatrics, University of California, San Diego; La Jolla, CA 92093, USA

[2]Department of Cellular & Molecular Medicine, University of California, San Diego; La Jolla, CA 92093, USA

[3]Center on Human Development & Disability, University of Washington, Seattle, WA 98195, USA

[4]Department of Neurology, University of Washington, Seattle, WA 98195, USA

[5]Department of Neurosciences, University of California, San Diego; La Jolla, CA 92093, USA

[6]Division of Biological Sciences, University of California, San Diego; La Jolla, CA 92093, USA

[7]Institute for Genomic Medicine, University of California, San Diego; La Jolla, CA 92093, USA

[8]Sanford Consortium for Regenerative Medicine, University of California, San Diego; La Jolla, CA 92093, USA

[9]Rady Children's Hospital, San Diego, CA 92123, USA

Abstract

Macroautophagy (hereafter autophagy) is a key pathway in neurodegeneration. Despite protective actions, autophagy may contribute to neuron demise, when dysregulated. Here we considered X-linked spinal and bulbar muscular atrophy (SBMA), a repeat disorder caused by polyglutamine-expanded androgen receptor (polyQ-AR). We found that polyQ-AR reduced long-term protein turnover and impaired autophagic flux in motor neuron-like cells. Ultrastructural analysis of SBMA mice revealed a block in autophagy pathway progression. We considered the transcriptional regulation of autophagy, and observed a functionally significant physical interaction between transcription factor EB (TFEB) and AR. Normal AR promoted, but polyQ-AR interfered with TFEB transactivation. To evaluate physiological relevance, we reprogrammed patient fibroblasts to induced pluripotent stem cells, and then to neuronal precursor cells (NPCs). We compared multiple SBMA NPC lines, and documented metabolic and autophagic flux defects

Users may view, print, copy, and download text and data-mine the content in such documents, for the purposes of academic research, subject always to the full Conditions of use:http://www.nature.com/authors/editorial_policies/license.html#terms

Corresponding author: Albert La Spada, MD, PhD, Cellular & Molecular Medicine, Neurosciences, and Pediatrics, University of California, San Diego, 9500 Gilman Drive, MC 0642, La Jolla, CA 92093-0642, (858)-246-0148 [ph.], alaspada@ucsd.edu.

*These authors contributed equally to this work.

Author Contributions: C.J.C., H.C.M., H.F., Y.B., J.E.Y., A.R.M., G.A.G. & A.R.L. designed the experiments. C.J.C., H.C.M., H.F., Y.B., J.E.Y., A.L., N.I., B.L.S., C.C. & G.A.G. performed the experiments. C.J.C., H.C.M., H.F., Y.B., J.E.Y., A.R.M., G.A.G. & A.R.L. analyzed the data. C.J.C., H.C.M., G.A.G. & A.R.L. wrote the manuscript.

Author Manuscript Author Manuscript Author Manuscript Author Manuscript

that could be rescued by TFEB. Our results indicate that polyQ-AR diminishes TFEB function to impair autophagy and promote SBMA pathogenesis.

Introduction

As post-mitotic cells incapable of rapid self-renewal, neurons are exquisitely susceptible to different types of cell stress; hence, maintenance of protein quality control poses a special challenge for central nervous system (CNS) cells[1,2]. Macroautophagy (hereafter referred to as autophagy) is dedicated to recovery from nutrient stress in non-neural cells, but in neurons has been adapted to degrade misfolded proteins and dysfunctional organelles[3]. The current view of neuronal autophagy is that of a pro-survival response that counters aggregate-prone proteins, as basal autophagy is crucial for normal CNS function[4,5], and autophagy can promote clearance of aggregate-prone proteins and improve disease in mouse and fly models of neurodegeneration[4,6,7]. The autophagy pathway involves the *de novo* synthesis of a double-membrane bound structure (the autophagosome) that sequesters cytoplasmic contents and delivers them to the lysosome for degradation[8]. Based upon studies done in yeast, initiation and promotion of autophagy are regulated by a family of 'Atg' genes that respond to specific signals[9]. In non-neural cells, nutrient deprivation drives the autophagy pathway ("starvation-induced autophagy"), but, in neurons, up-regulation of "quality control" autophagy occurs in response to accumulating aggregate-prone proteins that impair the ubiquitin-proteasome system[10].

Neurons exhibit a high rate of basal autophagy, and lysosome-mediated autophagosome turnover occurs rapidly[11,12]. In neurodegenerative disease, autophagic vesicles often accumulate, indicative of a pronounced impairment in neuronal autophagy. For example, in Alzheimer's disease (AD), immuno-electron microscopy analysis of AD patient brains revealed striking accumulations of autophagic vacuoles in the cell bodies and axons of cortical neurons[13]. Similar alterations in the autophagy pathway have been reported in Huntington's disease (HD) and Parkinson's disease (PD)[14]. This suggests that autophagy dysfunction is a common feature in neurodegenerative proteinopathies. However, whether autophagic vacuole accumulations reflect an initial neuroprotective response, or result from defective autophagy induction and progression remains unclear. Indeed, autophagy itself is a target in neurodegeneration, as a number of disease proteins, such as huntingtin, α-synuclein and presenilins, are directly involved in key steps of the autophagy pathway, including cargo recognition, autophagosome – lysosome fusion, and autophagosome cargo clearance[14], suggesting that loss-of-autophagy-function is a central feature of neurodegenerative disease.

In 2009, the Coordinated Lysosomal Enhancement and Regulation (CLEAR) gene network emerged as a novel nucleus-to-lysosome signaling axis that controls lysosome function[15]. The basic helix-loop-helix Transcription Factor E-B (TFEB) acts as a master regulator of the CLEAR network, and its targets include genes that encode Atg proteins, vesicular trafficking proteins, lysosomal enzymes, and lysosomal structural proteins[15,16]. Thus, TFEB is a key node in the transcriptional regulation of the autophagy-lysosome pathway, and numerous studies have documented that modulation of TFEB activity can ameliorate neurodegenerative disorders and lysosomal storage diseases characterized by neurological

Author Manuscript Author Manuscript Author Manuscript Author Manuscript

dysfunction[15-18]. In agreement with this work, recent evidence has uncovered an important role for TFEB dysfunction in neurodegeneration. As a master regulator of the CLEAR network, interference with TFEB signaling can lead to impaired autophagy function and diminished lysosomal degradative capacity, undermining neuronal survival. Indeed, reduced PGC-1α induction of TFEB expression in HD transgenic mice contributes to the aggregate clearance defects, neurological abnormalities, and neurodegeneration in this model[17]. In PD, α-synuclein neurotoxicity may also involve TFEB dysregulation, as degenerating dopaminergic neurons accumulate TFEB in the cytosol, resulting in reduced autophagy-lysosome pathway function[18]. Importantly, TFEB up-regulation in these studies was sufficient to rescue neurodegenerative phenotypes, confirming a key role for impaired TFEB action in HD and PD pathogenesis, and linking TFEB to the mechanistic basis of autophagy dysfunction in neurodegeneration.

Spinal and bulbar muscular atrophy (SBMA), also known as Kennedy's disease, is an X-linked inherited neuromuscular disorder characterized by lower motor neuron degeneration leading to weakness and atrophy of bulbar, facial, and limb muscles. SBMA patients display signs of androgen insensitivity with full disease penetrance restricted to adult males[19]. The causative mutation in SBMA is a CAG trinucleotide repeat expansion in the first exon of the androgen receptor (AR) gene[20]. This mutation encodes an extended polyglutamine (polyQ) stretch in the translated AR protein, and thus defines SBMA as one member of a family of nine polyQ repeat disorders, including HD, dentatorubral-pallidoluysian atrophy, and six forms of spinocerebellar ataxia[21]. AR is a transcription factor that controls the expression of androgen-responsive genes upon ligand-mediated nuclear translocation[22]. In SBMA, disease pathogenesis likely involves two distinct pathways: 1) gain-of-function toxicity due to production of misfolded polyQ-AR protein, and 2) loss, or alteration, of AR normal function[23].

In this study, we examined autophagy dysregulation in SBMA by analyzing multiple *in vivo* and *in vitro* models, including a human SBMA stem cell model, derived from induced pluripotent stem cells (iPSCs) reprogrammed from patient fibroblasts. These investigations revealed abnormalities of autophagic vacuole maturation and fusion with lysosomes in SBMA cell culture models, transgenic mice, and iPSC-derived neuronal precursor cells (NPCs), and enabled us to link impaired autophagy pathway dysfunction to the onset of SBMA disease phenotypes. After demonstrating a physical and functional interaction between AR and TFEB, we detected polyQ-AR interference with TFEB transactivation, and determined that TFEB dysregulation accounts for autophagic flux defects present in both SBMA motor neuron-like cells and patient NPCs. Our findings thus reveal altered autophagy onset as a crucial turning point in the SBMA pathogenic cascade, and implicate TFEB as a target for therapeutic intervention in this motor neuron disease.

Results

Polyglutamine-expanded AR protein impairs autophagic flux

To determine the effect of polyQ-expanded AR protein on proteostasis, we examined rates of long-lived protein turnover in motor neuron-like MN-1 cells that stably express normal AR with 24 glutamines (MN-1 AR24Q) or mutant AR with 65 glutamines (MN-1 AR65Q).

Author Manuscript Author Manuscript Author Manuscript Author Manuscript

Whereas short-lived protein turnover is primarily mediated by the ubiquitin-proteasome system (UPS), long-lived protein turnover is mainly attributed to the autophagy-lysosome pathway[9]. To quantify long-lived protein turnover, we labeled newly synthesized proteins with the non-radioactive methionine analog, L-azidohomoalanine (AHA), and measured rates of protein degradation after AHA-washout. We found that MN-1 AR65Q cells display reduced long-lived protein turnover (Supplementary Fig. 1).

Functional autophagy progression (i.e. "autophagic flux") requires that autophagosomes fuse with lysosomes, thereby ensuring that engulfed cargoes are efficiently degraded. To directly assess autophagic flux in MN-1 cells, we used a tandem tagged mCherry-EGFP-LC3 vector. Upon autophagosome formation, LC3 is incorporated into autophagosome membranes and both fluorescent tags are active, producing yellow puncta in merged images. When autophagosomes fuse with lysosomes, vesicle pH becomes acidic, quenching the EGFP signal so that only mCherry fluorescence remains detectable. This acidification-dependent change in fluorescence emission can be used to monitor autophagosome maturation. We thus tested the effect of AR protein expression on autophagic flux by transfecting MN-1 cells with the mCherry-EGFP-LC3 construct, and observed a marked increase in the number of autophagosomes per cell in both MN-1 AR24Q cells and MN-1 AR65Q cells, though autophagosome number was significantly higher in MN-1 AR65Q cells, and autolysosome number was correspondingly lower in MN-1 AR65Q cells (Fig. 1a). To exclude altered expression of the mCherry-EGFP-LC3 vector as a possible explanation, we transfected a mouse embryonic fibroblast (MEF) cell line, stably expressing mCherry-GFP-LC3, with AR25Q-BFP or AR125Q-BFP, and observed similar results (Fig. 1b). Next, we directly measured autophagy degradation function by analyzing the flux through the pathway, and measured changes in LC3-II levels relative to β-actin (Fig. 1c). When we analyzed LC3-II levels after ammonium chloride treatment, we observed reduced autophagic flux for MN-1 AR65Q cells (Fig. 1d), which is indicative of inefficient turnover of newly formed autophagosomes. Autophagic flux can also be assayed by measuring levels of p62, a protein adaptor of autophagic cargo to autophagosome membranes, and marker of autophagy pathway activity[24]. Inhibiting lysosome function with ammonium chloride increased p62 levels (Fig. 1e). Following ammonium chloride washout, p62 immunoblot analysis revealed that control MN-1 cells and MN-1 AR24Q cells could normalize p62 levels, suggesting competent lysosomal degradation of accumulated cargo. However, p62 levels remained elevated in MN-1 AR65Q cells (Fig. 1e), yielding impaired recovery after ammonium chloride treatment (Fig. 1f), indicative of impaired autophagic flux. Taken together, these data indicate autophagy pathway dysfunction in the presence of polyQ-AR.

Autophagy pathway is blocked in symptomatic SBMA mice

To evaluate the physiological relevance of autophagic flux defects observed in MN-1 cells, we performed ultrastructural analysis of autophagy pathway status in lumbar motor neurons from AR YAC CAG100 (YAC AR100) transgenic mice and AR YAC CAG20 (YAC AR20) transgenic control mice[25]. Male YAC AR100 mice recapitulate key features of SBMA, developing a progressive neuromuscular phenotype accompanied by motor neuron degeneration, while male YAC AR20 mice do not develop disease. We selected two time points for this study: a presymptomatic time point at which YAC AR100 mice do not

Author Manuscript Author Manuscript Author Manuscript Author Manuscript

display any neurological or cellular abnormalities (6 months), and a symptomatic time point by which YAC AR100 mice display a pronounced neuromuscular phenotype (14 months). To evaluate autophagosome maturation in SBMA mice, we generated electron micrographs of motor neurons from age-matched non-transgenic, YAC AR20, and YAC AR100 male littermates, and reviewed these micrographs for the presence of autophagosomes (APs) and autolysosomes (ALs), using established morphological criteria (Supplementary Fig. 2). Electron microscopy remains the gold standard for autophagy analysis, as it allows for direct observation of autophagic vesicles at different stages of maturation[24]. At 6 months, non-transgenic, YAC AR20, and YAC AR100 mice displayed comparable numbers of APs/motor neuron field, but YAC AR20 and YAC AR100 motor neurons contained greater numbers of ALs compared to controls, with many AR100 motor neurons containing remarkably high numbers of ALs (Fig. 2a). However, at 14 months of age, YAC AR100 motor neurons displayed numerous APs, in contrast to non-transgenic and YAC AR20 motor neurons, where the AL : AP ratio was much greater (Fig. 2b).

To quantify autophagy pathway progression in SBMA mice, we counted numbers of APs and ALs per motor neuron field. At 6 months of age, APs are comparable in frequency, but become markedly increased in motor neurons from YAC AR20 and YAC AR100 mice at 14 months (Fig. 3a). In 6 month-old mice, YAC AR100 motor neurons contained more ALs than YAC AR20 motor neurons, and significantly more than non-transgenic controls (Fig. 3b). At 14 months, YAC AR20 mice still showed proportionately more ALs than non-transgenic controls, but AL counts in YAC AR100 motor neurons were significantly decreased, appearing instead comparable to non-transgenic motor neurons (Fig. 3b). To evaluate autophagic flux, we reasoned that the ratio of ALs : APs serves as a gauge of autophagosome maturation and autophagy pathway progression, so we compared AL : AP ratios in SBMA transgenic mice. We found that the AL : AP ratio (which we designated the “autophagy index”) was increased in YAC AR100 motor neurons at 6 months of age (Fig. 3c). At 14 months of age, however, a significant reduction in the autophagy index was apparent in YAC AR100 motor neurons (Fig. 3c). The inability of YAC AR100 mice to maintain autophagy progression in the face of a persistent misfolded protein insult, as reflected by reduced AL formation at the symptomatic stage, may thus contribute to the pronounced motor neuron disease and progressive neural dysfunction seen in SBMA mice.

Impaired TFEB action underlies SBMA autophagy dysfunction

We hypothesized that autophagy pathway dysfunction in SBMA may result from altered transcription, as transcription dysregulation is a common pathology in polyQ disorders involving disease proteins that are transcription factors[21]. This led us to examine if polyQ-AR might be interfering with transcription factor E-B (TFEB), a master regulator of autophagy[16]. To evaluate this hypothesis, we tested for a physical interaction between TFEB and AR by performing co-immunoprecipitation (co-IP) assays in HEK293 cells co-transfected with TFEB and AR25Q or AR125Q. When we IP'd TFEB and immunoblotted with an anti-AR antibody, we detected both AR25Q and AR125Q (Fig. 4a), demonstrating an interaction between TFEB and AR. To determine if this physical interaction has functional significance, we transfected control MN-1 WT, MN-1 AR24Q, and MN-1 AR65Q cells with a 4X-CLEAR luciferase reporter construct, as CLEAR corresponds to the

Author Manuscript Author Manuscript Author Manuscript Author Manuscript

TFEB response element in the promoters of TFEB target genes[15]. We treated MN-1 cells bearing the 4X-CLEAR reporter with sucrose, which causes osmotic stress resulting in lysosomal activation via TFEB transactivation. Although sucrose yielded significant increases in 4X-CLEAR reporter activity in both control and AR24Q MN-1 cells, sucrose treatment did not elicit any transactivation response in MN-1 AR65Q cells (Fig. 4b). We then treated MN-1 cells with the lysosomal inhibitor ammonium chloride, which also promotes TFEB transactivation, and measured the expression level of TFEB target genes. We observed expression increases for TFEB target genes in both control MN-1 and MN-1 AR24Q cells, as expected, but did not detect appreciable changes in the expression of these targets in MN-1 AR65Q cells (Fig. 4c). One noteworthy outcome of both the sucrose challenge and ammonium chloride treatment was the potent effect of normal AR24Q protein on induction of 4X-CLEAR activity and TFEB target genes, as AR24Q promoted significantly higher levels of 4X-CLEAR activity at baseline and upon sucrose challenge in comparison to MN-1 WT cells that do not over-express AR (Fig. 4b), and AR24Q expression yielded much higher levels of induction for two of the TFEB target genes (Fig. 4c). These findings indicate that AR may act as a positive regulator of TFEB transactivation competence, suggesting that AR is a co-activator for TFEB. To assess the physiological relevance of these findings, we derived embryonic day 13 (E13) motor neurons from YAC AR20 and YAC AR100 transgenic mice, and obtained both spinal cord samples and quadriceps muscle samples from symptomatic 14 month-old YAC AR100 transgenic mice and matched controls. After RNA isolation, we interrogated the expression levels of various TFEB target genes by RT-PCR analysis. We observed significant reductions in gene expression for TFEB targets in isolated YAC AR100 E13 motor neurons (Fig. 4d), but did not detect any differences in TFEB target genes in transgenic spinal cord lysates, likely due to the fact that motor neurons comprise less than 5% of the cells contained in this sample type. Interestingly, similar to what we observed in MN1 AR24Q cells, over-expression of normal AR in YAC AR20 motor neurons elicited robust induction of two TFEB target genes, comparable to or exceeding that of non-transgenic control motor neurons (Fig. 4d). RT-PCR analysis of quadriceps muscle, however, yielded evidence for dramatic up-regulation of TFEB target genes in YAC AR100 mice (Supplementary Fig. 3), which is consistent with studies of SBMA knock-in mice [26], and indicative of a muscle-specific process of supraphysiological induction of TFEB in diseased muscle cells in SBMA.

To determine if TFEB transcription interference accounts for autophagy dysregulation in the SBMA MN-1 cell model, we transfected control MN-1 WT cells, MN-1 AR24Q cells, and MN-1 AR65Q cells with a blue fluorescent protein (BFP)-tagged TFEB expression vector or BFP empty vector, along with the 4X-CLEAR luciferase reporter, and noted marked increases in 4X-CLEAR reporter activity in all cases (Fig. 5a). To assess if TFEB over-expression can rescue impaired TFEB transactivation, MN-1 AR65Q cells expressing the 4X-CLEAR reporter were exposed to starvation stress, rapamycin, or ammonium chloride treatment. MN-1 AR65Q cells expressing BFP-TFEB displayed increased induction of 4X-CLEAR reporter activity in response to all three TFEB inducers, compared to MN-1 AR65Q cells transfected with BFP empty vector (Fig. 5b). In light of these results, we determined if TFEB up-regulation would rescue diminished autophagic flux in MN-1 AR65Q cells using the mCherry-GFP-LC3 assay. We began by transfecting MN-1 WT cells with the BFP-

Author Manuscript Author Manuscript Author Manuscript Author Manuscript

TFEB vector and observed increased numbers of autolysosomes, validating our TFEB construct and confirming the responsiveness of MN-1 cells to TFEB up-regulation (Supplementary Fig. 4). Although MN-1 AR65Q cells expressing BFP empty vector exhibited similar frequencies of autophagosomes and autolysosomes compared to untransfected MN-1 AR65Q cells, MN-1 AR65Q cells expressing BFP-TFEB displayed improved autophagic flux (Fig. 5c-d). These results suggest that TFEB dysfunction may account for the impaired autophagy pathway progression observed in multiple SBMA models.

AR functions as a co-activator of TFEB

As our findings indicate that wild type AR positively co-regulates TFEB, suggesting that AR could be a *bona fide* co-activator of TFEB, we chose to further explore the nature of the physical and functional interaction between AR and TFEB. Using a set of AR N-terminal and C-terminal deletion constructs (Fig. 6a), we performed co-transfections of different AR constructs with TFEB in HEK293 cells, and mapped the TFEB interaction domain on AR to its extreme C-terminal region (Fig. 6b-c). As entry of TFEB into the nucleus is required for transactivation of its target genes, and inhibitory regulation of TFEB by phosphorylation restricts TFEB to the cytosol [27], we tested if AR activation by its ligand affects TFEB subcellular localization. In MN-1 cells over-expressing AR with a normal glutamine tract, addition of the synthetic ligand R1881 resulted in localization of TFEB to the nucleus (Fig. 6d-e). This effect was AR-dependent, as MN-1 WT cells that do not over-express AR, did not exhibit this effect. Similarly, R1881 treatment of MN-1 65Q cells did not alter TFEB subcellular localization (Fig. 6d-e), indicating that polyQ-AR co-activation of TFEB is impaired. To further examine the ability of normal AR to promote TFEB transactivation, we transfected wild-type MN-1 cells with either an AR25Q-BFP expression construct or BFP empty vector in the presence of the 4X-CLEAR luciferase reporter, and we observed significantly higher induction of 4X-CLEAR luciferase activity in AR25Q-expressing cells at baseline, and upon ammonium chloride or rapamycin treatment (Fig. 6f). We then performed the opposite experiment, and knocked down AR in MN-1 AR24Q cells, achieving at least 50% protein knock-down. We observed a moderate reduction in 4X CLEAR luciferase activity upon AR shRNA knock-down at baseline, but noted a marked decrease in 4X CLEAR luciferase activity upon AR shRNA knock-down in rapamycin-treated MN-1 AR24Q cells (Fig. 6g). While the reduction in 4X-CLEAR reporter activity upon AR shRNA knock-down was only moderate at baseline, when we measured TFEB target gene expression in MN-1 24Q cells subjected to AR knock-down, we documented significant reductions in the expression levels of all tested TFEB targets (Fig. 6h). All of these studies suggest that AR functions as a TFEB co-activator.

TFEB rescues autophagy defects in SBMA stem cell model

Using retroviral transduction as previously described[28], primary fibroblasts from three different SBMA patients and three different healthy controls were reprogrammed to induced pluripotent stem cells (iPSCs). We established at least three clone lines / patient (Supplementary Fig. 5), and confirmed that all derived clones demonstrate key characteristics of embryonic stem cells (Supplementary Fig. 6a-c). To determine if our stem cell models retain disease-specific features, we sequenced the AR CAG repeat regions of 22

Author Manuscript Author Manuscript Author Manuscript Author Manuscript

iPSC clones and their six progenitor fibroblast cell lines, and confirmed that CAG repeat alleles remain virtually unchanged in size. We then generated neuronal precursor cells (NPCs) by collecting neural rosettes from plated embryoid bodies, as previously described[29]. NPC status was confirmed by detection of Nestin and Sox2 (Supplementary Fig. 6d). To determine if NPCs derived from SBMA patients retain disease-specific phenotypes, we performed filter trap assays, and detected accumulation of insoluble AR protein in SBMA NPC samples (Fig. 7a). Another established feature of SBMA is mitochondrial dysfunction, as expression of polyQ-AR in neuron-like cells yields mitochondrial membrane depolarization [30]. To evaluate mitochondrial function in the NPC lines, we exposed the different NPC clones to JC-1 dye and assessed mitochondrial membrane potential as a function of red : green fluorescence intensity (Supplementary Fig. 7). We found that about twice as many SBMA NPCs contain depolarized mitochondria in comparison to control NPCs (Fig. 7b). This striking result occurred at baseline, without subjecting NPCs to any insult, and was disease-specific.

After confirming that SBMA-derived NPCs encode polyQ-expanded AR proteins resistant to degradation, we evaluated the NPC lines for autophagy pathway function with the mCherry-EGFP-LC3 assay. As generation of iPSC lines and NPC derivatives is often associated with a high degree of clonal variability[31], we examined autophagic flux in three different clonal lines per patient (Supplementary Fig. 5). We found that SBMA NPCs display an increased frequency of autophagosomes in comparison to control NPCs (Fig. 7c-d). We calculated the autophagy index for control and SBMA NPCs, and noted a roughly 50% reduction in the autophagy index for SBMA NPCs, confirming that autophagic flux is impaired in SBMA NPCs, in agreement with SBMA cell culture and mouse models. When we measured the expression of TFEB target genes, we observed marked reductions in TFEB targets in SBMA NPCs (Fig. 7e). Co-IP experiments confirmed a physical interaction between TFEB and AR in both control and SBMA NPCs (Fig. 8a).

To determine if decreased TFEB function contributes to autophagy dysregulation and mitochondrial dysfunction in SBMA NPCs, we tested if TFEB over-expression could rescue these phenotypes. We began by transfecting control NPCs with BFP-empty vector and BFP-TFEB, and we noted a trend toward increased autolysosome formation and flux (Supplementary Fig. 8). We then transfected SBMA NPCs with BFP-TFEB, treated them with JC-1 dye, and determined mitochondrial membrane polarization by analyzing red : green fluorescence intensity. Importantly, up-regulation of TFEB significantly reduced the percentage of SBMA NPCs with depolarized mitochondria (Fig. 8b). We also repeated the autophagic flux assay, and found that TFEB over-expression promoted autophagic flux (Fig. 8c), yielding a significant reduction in autophagosomes and a modest increase in autolysosomes in SBMA NPCs (Fig. 8d). Calculation of the autophagy index yielded a five-fold increase for SBMA NPCs expressing TFEB. Hence, the effect of TFEB on autophagic vesicle profiles translated into a marked increase in the autophagy index for TFEB-expressing SBMA NPCs, demonstrating that TFEB over-expression virtually abolished the SBMA autophagic flux defect.

Author Manuscript Author Manuscript Author Manuscript Author Manuscript

Discussion

Autophagy has emerged as a key pathway in neurodegenerative disease, and has a role in maintaining normal neural function by degrading aggregate-prone proteins – even when neurons are not exposed to mutant misfolded peptides or increased levels of altered conformers[4,5]. Despite its clearly demonstrated protective actions, the capacity of the autophagy pathway for handling proteotoxic insults, such as polyQ disease proteins, is limited. Although autophagy is widely accepted as a crucial factor in the response of the CNS to misfolded protein stress, many unanswered questions remain: When in the course of a neurodegenerative proteinopathy does the autophagy pathway fail to operate properly? What step(s) in the autophagy pathway are the first to be blocked in neurodegenerative disease? With these key questions in mind, we studied autophagy dysfunction in a SBMA mouse model, immortalized cell line model, and a human iPSC-based stem cell model. Our results offer novel insights into the mechanistic basis of autophagy dysfunction in SBMA and related neurodegenerative proteinopathies.

Our findings identify a block in the fusion of autophagosomes with lysosomes as a likely cause of the autophagy dysfunction in SBMA. Ultrastructural analysis of SBMA motor neurons indicated that induction of autophagy is intact, if not markedly increased in the face of AR polyQ proteotoxic stress. Hence, in the case of AR polyQ stress, there is no evidence for reduced activation of the autophagy pathway, as shown for the related polyQ disorder HD, where sequestration of mTOR by polyQ-huntingtin has been reported[7]. Rather, AR neurotoxicity involves a block in autophagy pathway progression, similar to that observed in AD, where there is a striking accumulation of immature autophagic vesicles in patients' dystrophic neurites[13]. To delineate the basis of this effect, we considered the transcriptional regulation of the autophagy pathway, because transcription interference is a feature of polyQ diseases involving disease proteins that are transcription factors. One possibility, suggested by recent work on lysosome biogenesis[15], is that polyQ-expanded AR could interfere with TFEB-dependent transcription. As we, and others, have documented AR transcription dysregulation both *in vitro* and *in vivo*[23,25,32,33], and TFEB and AR share common sumoylation regulatory pathways and presumably co-factors[34], we undertook a thorough analysis of TFEB function in SBMA. Our results strongly suggest that TFEB dysregulation, mediated by an inhibitory interaction with polyQ-expanded AR, is responsible for autophagic flux impairments present in SBMA models.

In addition to demonstrating polyQ-expanded AR interference with TFEB transactivation, our data suggests that AR can normally interact with TFEB to promote its function. We found evidence for an interaction between normal Q-length AR and TFEB in both over-expression systems and under endogenous conditions, and we report enhanced TFEB signaling and increased autophagy pathway activity when normal AR protein is over-expressed. When we mapped the TFEB interaction domain on AR, we localized the interaction domain to the C-terminal 180 amino acids. This region of AR comprises the bulk of the AF-2 activation domain, a highly conserved region that serves as a binding pocket for steroid receptor co-activator (SRC) proteins [35]. These findings suggest that AR and TFEB may normally exist in the same protein complex, and that AR and TFEB may require shared co-activator proteins for optimal transactivation function. Hence, AR activation may

Author Manuscript Author Manuscript Author Manuscript Author Manuscript

promote TFEB transactivation through recruitment of certain co-activator proteins, but upon polyQ tract expansion, mutant AR may no longer maintain the proper dynamics of protein-protein interactions within the complex, resulting in diminished TFEB transactivation competence. Altered TFEB protein-protein interactions in the presence of polyQ-expanded AR in the cytosol may thus block TFEB nuclear localization by preventing a translocation factor from properly interacting with TFEB, even when TFEB is dephosphorylated and primed for nuclear entry. Future studies aimed at defining the nature of the cytosolic TFEB protein complex in the presence of polyQ-expanded AR may reveal the TFEB interactors responsible for its translocation, and how inclusion of polyQ-expanded AR in the TFEB protein complex interferes with TFEB subcellular localization. Such a model of polyQ-expanded AR negatively altering the function of a protein with which it normally interacts is fully consistent with emerging views of polyQ disease pathogenesis, where studies of SCA1 have shown that polyQ-expanded ataxin-1 is less capable of promoting Capicua function than its normal Q-length counterpart, resulting in reduced Capicua transcriptional repressor activity[36]. As AR normally interacts with a number of transcription co-regulators, and studies of a SBMA fly model indicate that polyQ-expanded AR may promote neurotoxicity by reducing the function of the co-regulators with which it interacts[37], reduced availability of a co-activator protein, shared by AR and TFEB, may result in decreased TFEB transactivation function in SBMA. Our findings thus underscore the importance of disease protein normal function in delineating the mechanistic basis of the neurodegeneration in polyQ repeat disorders.

While induction of autophagy is initially protective in a primary neuron model of SBMA toxicity[38], and correspondingly over-expression of p62, beginning prior to disease onset, can ameliorate motor phenotypes and neuropathology in SBMA transgenic mice[39], our studies indicate that inhibition of autophagosome-lysosome fusion ultimately occurs in SBMA, impairing long-lived protein turnover and compromising cellular proteostasis. Analysis of SBMA mice revealed that properly functioning autophagy is evident at early time points in presymptomatic mice, but with disease progression, autophagy becomes dysfunctional and disease ensues. Our results also indicate that autophagy dysregulation differs between different cell types, as polyQ-AR inhibits TFEB function in the neuronal milieu, but can actually promote TFEB transactivation in skeletal muscle, which may yield excessive autophagy that can contribute to muscle atrophy [40]. As altered muscle physiology may initiate SBMA disease pathogenesis [41], understanding the connection and potential cross-talk between autophagy dysregulation in skeletal muscle and motor neurons will be an important goal of future research.

Modeling of neurodegenerative diseases using iPSCs derived from patient fibroblasts is emerging as a powerful technique for understanding disease pathogenesis[42]. In triplet repeat disorders, repeat instability during reprogramming is a potential concern in modeling these diseases using iPSC technology. In accordance with a recent study of HD, where perfect stability of the normal CAG repeat and only occasional minor changes in the expanded CAG repeat were observed[43], we documented repeat stability, with only very minor changes (1 – 2 repeats) in CAG allele size in iPSCs and NPCs upon reprogramming. Hence, our results, and those of another group working independently[45], confirm that CAG repeat length alteration is an infrequent event in SBMA stem cell modeling, and when it occurs, the

Author Manuscript Author Manuscript Author Manuscript Author Manuscript

observed changes are minor. In addition to tracking the sizes of CAG repeat alleles, we also examined SBMA iPSC-derived lines for disease-specific phenotypes. To do this, we performed filter trap assays and documented increased insoluble misfolded protein accumulations in NPC lines from SBMA patients. We also measured mitochondrial membrane potential, and noted that SBMA-derived NPCs are twice as likely to contain depolarized mitochondria in comparison to control NPCs, in agreement with studies of MN-1 and PC12 cells over-expressing polyQ-AR [30]. As the process of reprogramming can introduce genetic and molecular alterations to the resultant cell lines and thereby yield spurious phenotypes[31], we pursued SBMA stem cell model generation by utilizing three different, unrelated SBMA patients and three different controls, and we produced three unique iPSC clones per human fibroblast line to yield a collection of 18 different clonal lines. Although production and characterization of so many lines required considerable effort, analysis of multiple independent clones from multiple patients and controls is necessary to insure the validity of observed disease-specific phenotypes. Using this approach, we completed an extensive investigation of autophagic flux, and found evidence for SBMA-specific reductions in autophagic flux in NPCs, consistent with observations in MN-1 cells and SBMA transgenic mice. We then documented that TFEB could improve mitochondrial membrane polarization and relieve the autophagic flux blockage present in SBMA NPCs. During conditions of autophagic flux inhibiton, autophagic cargo (including depolarized mitochondria) accumulate, leading to increased reactive oxygen species production and decreased lysosome function. Thus, up-regulation of TFEB and activation of the CLEAR signaling network likely rescues the block in autophagic flux by promoting autophagy-lysosome pathway activity, and facilitating the clearance of defective mitochondria. Although iPSC-derived neural modeling documented accumulations of autophagic vacuoles and other abnormalities in a study of PD[47], to our knowledge, this is the first time that dynamic studies of autophagy pathway function in an iPSC-derived neural lineage yielded a quantifiable defect in autophagic flux. Hence, this work provides proof-of-principle for future efforts aimed at dissecting autophagy abnormalities in neurological diseases using a stem cell modeling approach.

Modulation of autophagy is being touted as a potential therapy for neurodegenerative proteinopathies, but the timing of autophagy activation and the ability of an intervention to enhance autophagic clearance must both be carefully considered, when designing treatment regimens. Indeed, further induction of dysfunctional autophagy may actually exacerbate cellular toxicity and paradoxically accelerate disease progression. Deconstructing the specific defects in the autophagy pathway in neurodegenerative proteinopathies and determining the impact of autophagy activation on documented alterations are required, before therapies can be envisioned. In our SBMA NPC model, we documented significant down-regulation of TFEB target genes in comparison to controls, and found that induction of TFEB activity completely reversed metabolic and autophagic flux phenotypes observed in SBMA-derived NPCs. In light of these results, TFEB is an attractive candidate for therapy development efforts. In addition to elevating the status of TFEB for therapy development, a representative stem cell model of SBMA will permit further study into the basis of disease pathogenesis. Another therapeutic application of the SBMA NPC model will be to develop it as a tool for identifying compounds that can correct autophagic flux defects, as high

Author Manuscript Author Manuscript Author Manuscript Author Manuscript

throughput screening for compounds capable of rescuing the autophagy pathway block in this model could be pursued in a high content format[48,49]. Compounds that favor autophagosome – lysosome fusion would be plausible therapies not only for SBMA, but also for related disorders characterized by impaired autophagy pathway progression.

Methods

DNA constructs

The AR-Q(n) expression constructs (where 'n' is the number of CAG repeats) have been described previously[38]. The mCherry-EGFP-LC3 construct was kindly provided by Dr. T. Johansen. The empty EBFP2 construct was obtained from Addgene, and from it, we derived BFP-TFEB, BFP-AR25Q, and BFP-AR125Q vectors. The TFEB expression construct was obtained from Origene. We generated a 4X-CLEAR element driven by the HTK promoter by subcloning into the PGL3 firefly luciferase vector (Promega).

Cell culture work

All cell culture lines were grown in complete DMEM (Life Technologies) with 10% FBS and 5 mM glutamine. Motor Neuron like (MN-1) AR24Q and AR65Q cells have been described previously[50]. Mixed primary motor neuron cultures were prepared from embryonic day 13 (E13) WT, YAC AR20, or YAC AR100 mice, as previously described[51]. All cell line and primary neuron transfections utilized Lipofectamine 2000, following the manufacturer's protocol (Life Technologies). Cells were treated with rapamycin 2 μM or ammonium chloride 20 mM, as indicated. Luciferase activity was measured using the Dual-Luciferase® Reporter Assay System (Promega). Briefly, for MN-1 cell transactivation assays, MN-1 cells were transfected with the 4X-CLEAR promoter-reporter construct, and CMV-promoter Renilla luciferase vector was used as the internal control. For Androgen Receptor knockdown, MN-1 AR24Q cells were transfected with AR shRNA (Santa Cruz, sc-29204) or scrambled control construct using the manufacturer's protocol. Twenty-four hrs after transfection, cells were treated overnight with indicated compounds and collected according to the manufacturer's instructions. Firefly and Renilla luciferase activity was measured using Glomax 96 microplate luminometer (Promega), and values were normalized to untreated MN-1 WT cells. All luciferase reporter assays were performed in triplicate or quadruplicate.

iPSC derivation and NPC experimentation

Fibroblasts were collected from dermal biopsies from 3 European Caucasian male SBMA patients between the ages of 55 and 65 years old and 3 European Caucasian male healthy donors between the ages of 38 and 65 years old upon informed consent in compliance with an UCSD-approved IRB protocol #130337ZF. Fibroblasts were cultured in Dulbecco's modified eagle medium (DMEM) (1×) with 10% (v/v) fetal bovine serum and 5% (v/v) antibiotics (Pen/Strep 10 000 U/ml). Low passage fibroblasts were reprogrammed as previously described[52]. Briefly, Oct4, c-Myc, Klf4, and Sox2 human cDNAs were obtained from Addgene and used in a retroviral system to infect fibroblasts[28]. Two days after infection, fibroblasts were transferred onto irradiated mouse embryonic fibroblasts (Chemicon) with hESC medium. After 10-15 days, hESC-like cells were manually selected

Author Manuscript Author Manuscript Author Manuscript Author Manuscript

and moved to feeder-free conditions on matrigel-coated dishes (BD Bioscience) with mTeSR1 (StemCell Technologies). Standard G-banding chromosome analysis of putative iPSC clones was performed by Children's Hospital Los Angeles (Los Angeles, CA). NPCs were obtained as previously described[52], with minor modifications. Briefly, iPSC media was removed and switched to DMEM/F12 (Invitrogen) with 1× N2 and 1 μM dorsomorphin (Calbiochem). After two days, the colonies were mechanically dissociated and kept under rotation for 5-7 days at 37°C to form embryoid bodies (EBs). The EBs were plated onto dishes coated with poly-ornithine/laminin (Sigma), where the rosettes would arise on the plates after 7 days. Manually collected neural rosettes were enzymatically dissociated and plated again to be expanded onto coated dishes with DMEM/F12 medium, enriched with 0.5X N2 / 0.5X B27 / FGF2. NPC transfections were performed using Amaxa Nucleofection kits (rat neural stem cell kit; Lonza) according to the manufacturer's instructions.

Subcellular fractionation and co-immunoprecipitation

Nuclear and cytosol fractionation was performed as previously described[16]. Briefly, attached NPCs in 6 cm dishes were washed with PBS previous to adding lysis buffer (50mM Tris-HCl, 0.5% triton, 137.5 mM NaCl, 10% glycerol, 5 mM EDTA) with protease inhibitors (Roche). The dish was incubated at 4°C in constant agitation for 15 min. The lysate was carefully collected to avoid breaking the nucleus and centrifuged. The supernatant represented the cytosolic fraction. The nuclear fraction was washed twice, and lysed upon the addition of 0.5% SDS, sonicated for 10 min, and centrifuged to eliminate cell debris. Protein levels were quantified and samples were prepared for immunoblotting as described above.

Cells were collected in IP buffer (PBS 0.1% TritonX100) and lysed by needling. After centrifugation to remove cell debris, 200 ug of protein lysates were prepared in a final volume of 200 ul. Thirty ul of Dynabeads (Life Technologies) were coated with TFEB antibody (Cell signaling #4240BC) or AR antibody (Santa Cruz H280 sc-13062) for 1 hr. Antibody-coated beads and lysate were incubated overnight at 4°C, and after 3 PBS washes, IP'd material was eluted in 20 ul of PBS 0.1% Triton-X100. Twenty ug of lysate were used as input controls.

Immunohistochemistry

Cells were plated into poly-D-lysine coverslips and fixed in 4% paraformaldehyde and permeabilized with 0.25% (v/v) Triton X-100 in PBS. Cells were then blocked in 3% (v/v) BSA (bovine serum albumin) in PBS. All steps included 3 washes of PBS in between. For subcellular localization studies, after transfection with 3x-Flag-TFEB, the testosterone analogue R1881 (1 nM) was added for 24 hrs. Cells were stained for TFEB (1:500, Alexa488) and Androgen Receptor (1:500, Alexa594), counterstained with Hoescht, and imaged in a confocal microscope. Over 100 TFEB positive (green) cells were scored for nuclear or cytosolic TFEB signal by a blinded observer. For NPCs, cells were plated in 4-well chamber slides coated with poly-ornithine/laminin (Sigma) with DMEM/F12 medium, enriched with 0.5X N2 / 0.5X B27 / FGF2. Primary antibodies used were Nanog (1:250, R&D Systems AF1997), Lin28 (1:250, R&D Systems AF3757); human Nestin (1:100, Chemicon mab5326); Sox2 (1:250, Cell Signaling 2748); Oct4 (1:250, Santa Cruz

Author Manuscript Author Manuscript Author Manuscript Author Manuscript

sc-365509). Images were taken using a Zeiss laser scanning inverted microscope and/or a Zeiss confocal microscope, and for mCherry-EGFP-LC3 analysis, blinded observers counted vesicle numbers in the mCherry (red), GFP (green), or merged (yellow) channels for 25 – 50 cells / condition. All experiments were done in triplicate or quadruplicate.

Mitochondrial Membrane Potential Assay

The mitochondrial membrane potential assay was conducted using image analysis in the NC-3000 (ChemoMetec – Denmark) system, which automatically detects cells with collapsed mitochondria membrane potential. Briefly, 1×10^6 cells were stained with JC-1 for 20 min. Stained cells were centrifuged and washed twice with PBS. Cells were then stained with DAPI for viability purposes. Cellular JC-1 monomers and aggregates are detected as green and red fluorescence respectively, with mitochondrial depolarization revealed as a decrease in red : green fluorescence intensity. After staining, cells are loaded into either of two types of ChemoMetec slides: the 2-chamber NC-Slide A2 or the 8-chamber NC-Slide A8. Samples were analyzed using the NC-3000 system and the amount of blue, green, and red fluorescence of individual cells was quantified. The intensity of red and fluorescence is shown in a scatter-plot, all experiments were done in triplicate and gating analysis was equal for all conditions, based upon the control.

DNA extraction and CAG repeat sizing

Genomic DNA extraction was performed using DNeasy Kit (Qiagen). Amplification of the CAG repeat site in the Androgen Receptor gene was performed using Fast Start PCR master mix kit (Roche). For the reaction, 100 ng of DNA was used as template and 10 nM of primers, forward (5′ TCC AGA ATC TGT TCC AGA GCG TGC 3′) and reverse (5′ GCT GTG AAG GTT GCT GTT CCT CAT 3′). PCR products were sequenced using reverse primer, and the quality of generated sequences was analyzed by Geospiza (http://www.geospiza.com/finchtv/).

RT-PCR analysis

Total RNA from MN-1 cells, E13 motor neurons, or SBMA mice was extracted using the Trizol method. cDNA was generated using SuperScript® III First-Strand Synthesis System (Life Technologies). For NPCs, total RNA extraction from EBs or NPCs was performed using the RNeasy kit (Qiagen). cDNA was generated with the High Capacity reverse transcription kit (Life Technologies). Quantification of mRNA was performed using an Applied Biosystems 7500 Real Time Sequence Detection System with ABI Assays-on-Demand primers and TaqMan® based probes. ABI TaqMan primer and probe set designations are available upon request. Relative fold change expression levels were calculated and normalized to controls, and all experiments were done in triplicate.

Immunoblotting analysis

Cells were harvested in RIPA lysis buffer (10mM Tris, 0.1% SDS, 1% SDOC, 0.01% TX-100, 150 mM NaCl) and homogenized by passing 5× through a 26.5 gauge syringe. Fifty μg protein lysates were run on Bis-Tris gel (Life Technologies) and transferred to PVDF membranes (Millipore) using a semi-dry transfer system (Life Technologies). The

Author Manuscript Author Manuscript Author Manuscript Author Manuscript

membranes were blocked with 5% non-fat dried milk RT for 1 hr, and then probed with rabbit anti-LC3 antibody (1:1500, Novus #2220), rabbit anti-p62 antibody (1:1000, MBL #PM045), rabbit anti-androgen receptor (1:2000, Santa Cruz H280 sc-13062), rabbit anti-TFEB (1:1000, Cell Signaling #4240BC), or mouse anti-beta actin antibody (1:2000, Abcam #8226) in 5% BSA at 4C overnight. After washing, membranes were incubated with HRP-secondaries (1:5000 Santa Cruz) in 5% Milk, PBS-T for 1 hr at RT. After treatment with enhanced ECL chemiluminescence (Upstate), the membranes were visualized by autoradiography. Filter trap assays were performed as described previously[17]. Cellulose acetate membranes (Whatman) were blotted overnight in constant agitation at 4°C with anti-AR antibodyN-20 (Santa Cruz sc-816; 1:500), followed by horseradish-peroxidase-conjugated secondary antibody (1:5,000; Santa Cruz), and then visualized using ECL chemiluminescence. For the subcellular fractionation, the PVDF membranes were analyzed using the Odyssey Western Blotting system (Li-Cor). The membrane was blotted overnight in constant agitation at 4°C with anti-TFEB (1:500; Cell Signaling), H3 (1:5000; Cell Signaling) and Lamp1 (1:1,000; Cell Signaling) followed by IRDye secondary antibody (1:10,000; Li-Cor), and then visualized with the Odyssey Infrared Imaging System (Li-Cor). All densitometry analysis was performed using NIH ImageJ software. For figures containing cropped gel blots, we have provided full length blots (Supplementary Figure 9).

Ultrastructural analysis

Male non transgenic, YAC AR20 or YAC AR100 mice (C57BL6/J background) (n = 3 – 4 / cohort) were sacrificed at 6 months and 14 months of age, and lumbar cord regions were processed as previously described 37. Semi-thin (1 μM) sections were stained with Richardson's and examined by light microscopy to assure cytological tissue quality. Sixty nm sequential sections were collected on coated copper or nickel 200 mesh grids, and then stained with lead citrate and uranyl acetate for contrast. Motor neurons were mapped out and photographed. Each section yielded an average of 7 motor neurons with 3 sections / individual. The sections were taken from 3 different blocks and thus represented the L3 – L5 region of the lumbar spinal cord. With a Philips TEM/CM 10 electron microscope, 50 – 60 motor neurons / cohort were photographed, scanned into Adobe Photoshop, and examined by 3 independent, blinded observers who had been trained to identify autophagic vacuoles and autolysosomes, based upon established criteria and sample images from the literature. Mice were kept in standard dark/light cycle conditions, and housed under standard requirements of rodent IACUC guidelines (n=3-4 individuals/cage). If isolation was required due to in-fighting, single housed animals were provided enrichment. All animal experiments were performed in accordance with institutional IACUC guidelines at the University of Washington and UCSD.

Long-lived protein turnover assay

We labeled nascent protein populations in MN-1 cells with the non-radioactive methionine analog L-azidohomoalanine (AHA) (Invitrogen), and chased with non-labeled media. Cell lysates were collected after 48 and 100 hrs for long-term protein clearance analysis. Briefly, equal amounts of lysate were run on a Western blot, and AHA-labeled protein populations were detected by biotin-alkyne reaction. The amount of labeled protein/lane/time point was quantified by densitometry (Image J), and linear fit curves over time were determined for

Author Manuscript Author Manuscript Author Manuscript Author Manuscript

each cell line. The slope of each curve was determined to be the rate of lysosomal-mediated long-lived protein turnover.

Statistical analysis

No statistical methods were used to determine sample sizes, but our samples sizes are similar to or exceed those reported in previous publications[28,41,53]. For the iPSC experiments, 10 to 12 clones were generated, and we randomly selected three different clones for each individual line to compensate for the high degree of clonal variability. A total of nine clones for the control group and ten clones for the SBMA group were analyzed in the autophagy flux assay, which is well in excess of previous publications in the field[45]. Autophagic flux data collection and analysis were performed blindly to the conditions of the experiment. For experiments utilizing mice, no randomization was required, as groups were generated based upon genotype status. All transgenic male animals were analyzed and their genotypes determined twice. Data distribution was assumed to be normal. All data were prepared for analysis with standard spreadsheet software (Microsoft Excel). All errors bars shown in the figures are s.e.m. Statistical analysis was done using Microsoft Excel, GraphPad Prism v5 or VassarStats website: (http://faculty.vassar.edu/lowry/VassarStats.html). For ANOVA analysis involving multiple sample comparisons, we performed post-hoc testing to discriminate significance relationships. For t-test analysis, we applied one-tailed tests for independent samples. A supplementary methods checklist for this paper is available online.

Supplementary Material

Refer to Web version on PubMed Central for supplementary material.

Acknowledgments

The authors wish to thank L.I. Macedo de Souza, A.C. Smith, and H. Burke for technical assistance, N. Mizushima and Z. Yue for providing GFP-LC3 transgenic mice, J.P. Taylor for supplying the mCherry-GFP-LC3 MEFs, and T. Johansen for the gift of the mCherry-EGFP-LC3 construct. This work was supported by grants from the National Institutes of Health (R01 NS041648 to A.R.L., R01 AG033082 to A.R.L., DP2-OD006495-01 to A.R.M.), the Muscular Dystrophy Association (Basic Research Grant to A.R.L., Development Grant to C.J.C., and Basic Research Grant to A.R.M.), and the California Institute for Regenerative Medicine (CIRM TR2-01814 to A.R.M.).

References

1. Malgaroli A, Vallar L, Zimarino V. Protein homeostasis in neurons and its pathological alterations. Curr Opin Neurobiol. 2006; 16:270–274. [PubMed: 16713705]
2. Taylor JP, Hardy J, Fischbeck KH. Toxic proteins in neurodegenerative disease. Science. 2002; 296:1991–1995. [PubMed: 12065827]
3. Levine B, Kroemer G. Autophagy in the pathogenesis of disease. Cell. 2008; 132:27–42. [PubMed: 18191218]
4. Hara T, et al. Suppression of basal autophagy in neural cells causes neurodegenerative disease in mice. Nature. 2006; 441:885–889. [PubMed: 16625204]
5. Komatsu M, et al. Loss of autophagy in the central nervous system causes neurodegeneration in mice. Nature. 2006; 441:880–884. [PubMed: 16625205]
6. Komatsu M, et al. Essential role for autophagy protein Atg7 in the maintenance of axonal homeostasis and the prevention of axonal degeneration. Proc Natl Acad Sci U S A. 2007; 104:14489–14494. [PubMed: 17726112]

Author Manuscript Author Manuscript Author Manuscript Author Manuscript

7. Ravikumar B, et al. Inhibition of mTOR induces autophagy and reduces toxicity of polyglutamine expansions in fly and mouse models of Huntington disease. Nat Genet. 2004; 36:585–595. [PubMed: 15146184]
8. Shintani T, Klionsky DJ. Autophagy in health and disease: a double-edged sword. Science. 2004; 306:990–995. [PubMed: 15528435]
9. Klionsky DJ. Autophagy: from phenomenology to molecular understanding in less than a decade. Nat Rev Mol Cell Biol. 2007; 8:931–937. [PubMed: 17712358]
10. Pandey UB, et al. HDAC6 rescues neurodegeneration and provides an essential link between autophagy and the UPS. Nature. 2007; 447:859–863. [PubMed: 17568747]
11. Mizushima N, Yamamoto A, Matsui M, Yoshimori T, Ohsumi Y. In vivo analysis of autophagy in response to nutrient starvation using transgenic mice expressing a fluorescent autophagosome marker. Mol Biol Cell. 2004; 15:1101–1111. [PubMed: 14699058]
12. Boland B, et al. Autophagy induction and autophagosome clearance in neurons: relationship to autophagic pathology in Alzheimer's disease. J Neurosci. 2008; 28:6926–6937. [PubMed: 18596167]
13. Nixon RA, et al. Extensive involvement of autophagy in Alzheimer disease: an immuno-electron microscopy study. Journal of neuropathology and experimental neurology. 2005; 64:113–122. [PubMed: 15751225]
14. Wong E, Cuervo AM. Autophagy gone awry in neurodegenerative diseases. Nat Neurosci. 2010; 13:805–811. [PubMed: 20581817]
15. Sardiello M, et al. A gene network regulating lysosomal biogenesis and function. Science. 2009; 325:473–477. [PubMed: 19556463]
16. Settembre C, et al. TFEB links autophagy to lysosomal biogenesis. Science. 2011; 332:1429–1433. [PubMed: 21617040]
17. Tsunemi T, et al. PGC-1alpha Rescues Huntington's Disease Proteotoxicity by Preventing Oxidative Stress and Promoting TFEB Function. Sci Transl Med. 2012; 4:142ra197.
18. Decressac M, et al. TFEB-mediated autophagy rescues midbrain dopamine neurons from alpha-synuclein toxicity. Proceedings of the National Academy of Sciences of the United States of America. 2013; 110:E1817–1826. [PubMed: 23610405]
19. Dejager S, et al. A comprehensive endocrine description of Kennedy's disease revealing androgen insensitivity linked to CAG repeat length. J Clin Endocrinol Metab. 2002; 87:3893–3901. [PubMed: 12161529]
20. La Spada AR, Wilson EM, Lubahn DB, Harding AE, Fischbeck KH. Androgen receptor gene mutations in X-linked spinal and bulbar muscular atrophy. Nature. 1991; 352:77–79. [PubMed: 2062380]
21. La Spada AR, Taylor JP. Repeat expansion disease: progress and puzzles in disease pathogenesis. Nat Rev Genet. 2010; 11:247–258. [PubMed: 20177426]
22. Cary GA, La Spada AR. Androgen receptor function in motor neuron survival and degeneration. Phys Med Rehabil Clin N Am. 2008; 19:479–494. viii. [PubMed: 18625411]
23. Thomas PS Jr, et al. Loss of endogenous androgen receptor protein accelerates motor neuron degeneration and accentuates androgen insensitivity in a mouse model of X-linked spinal and bulbar muscular atrophy. Hum Mol Genet. 2006; 15:2225–2238. [PubMed: 16772330]
24. Klionsky DJ, et al. Guidelines for the use and interpretation of assays for monitoring autophagy. Autophagy. 2012; 8:445–544. [PubMed: 22966490]
25. Sopher BL, et al. Androgen receptor YAC transgenic mice recapitulate SBMA motor neuronopathy and implicate VEGF164 in the motor neuron degeneration. Neuron. 2004; 41:687–699. [PubMed: 15003169]
26. Chua JP, et al. Transcriptional activation of TFEB/ZKSCAN3 target genes underlies enhanced autophagy in spinobulbar muscular atrophy. Hum Mol Genet. 2014; 23:1376–1386. [PubMed: 24150846]
27. Martina JA, Chen Y, Gucek M, Puertollano R. MTORC1 functions as a transcriptional regulator of autophagy by preventing nuclear transport of TFEB. Autophagy. 2012; 8:903–914. [PubMed: 22576015]

Author Manuscript Author Manuscript Author Manuscript Author Manuscript

28. Takahashi K, Yamanaka S. Induction of pluripotent stem cells from mouse embryonic and adult fibroblast cultures by defined factors. Cell. 2006; 126:663–676. [PubMed: 16904174]
29. Marchetto MC, et al. A model for neural development and treatment of Rett syndrome using human induced pluripotent stem cells. Cell. 2010; 143:527–539. [PubMed: 21074045]
30. Ranganathan S, et al. Mitochondrial abnormalities in spinal and bulbar muscular atrophy. Hum Mol Genet. 2009; 18:27–42. [PubMed: 18824496]
31. Boulting GL, et al. A functionally characterized test set of human induced pluripotent stem cells. Nat Biotechnol. 2011; 29:279–286. [PubMed: 21293464]
32. Lieberman AP, Harmison G, Strand AD, Olson JM, Fischbeck KH. Altered transcriptional regulation in cells expressing the expanded polyglutamine androgen receptor. Hum Mol Genet. 2002; 11:1967–1976. [PubMed: 12165558]
33. McCampbell A, et al. CREB-binding protein sequestration by expanded polyglutamine. Hum Mol Genet. 2000; 9:2197–2202. [PubMed: 10958659]
34. Miller AJ, Levy C, Davis IJ, Razin E, Fisher DE. Sumoylation of MITF and its related family members TFE3 and TFEB. J Biol Chem. 2005; 280:146–155. [PubMed: 15507434]
35. He B, Kemppainen JA, Voegel JJ, Gronemeyer H, Wilson EM. Activation function 2 in the human androgen receptor ligand binding domain mediates interdomain communication with the NH(2)-terminal domain. J Biol Chem. 1999; 274:37219–37225. [PubMed: 10601285]
36. Lam YC, et al. ATAXIN-1 interacts with the repressor Capicua in its native complex to cause SCA1 neuropathology. Cell. 2006; 127:1335–1347. [PubMed: 17190598]
37. Nedelsky NB, et al. Native functions of the androgen receptor are essential to pathogenesis in a Drosophila model of spinobulbar muscular atrophy. Neuron. 2010; 67:936–952. [PubMed: 20869592]
38. Young JE, et al. Polyglutamine-expanded androgen receptor truncation fragments activate a Bax-dependent apoptotic cascade mediated by DP5/Hrk. J Neurosci. 2009; 29:1987–1997. [PubMed: 19228953]
39. Doi H, et al. p62/SQSTM1 differentially removes the toxic mutant androgen receptor via autophagy and inclusion formation in a spinal and bulbar muscular atrophy mouse model. J Neurosci. 2013; 33:7710–7727. [PubMed: 23637164]
40. Bonaldo P, Sandri M. Cellular and molecular mechanisms of muscle atrophy. Dis Model Mech. 2013; 6:25–39. [PubMed: 23268536]
41. Cortes CJ, et al. Muscle expression of mutant androgen receptor accounts for systemic and motor neuron disease phenotypes in spinal and bulbar muscular atrophy. Neuron. 2014; 82:295–307. [PubMed: 24742458]
42. Marchetto MC, Brennand KJ, Boyer LF, Gage FH. Induced pluripotent stem cells (iPSCs) and neurological disease modeling: progress and promises. Human molecular genetics. 2011; 20:R109–115. [PubMed: 21828073]
43. Induced pluripotent stem cells from patients with Huntington's disease show CAG-repeat-expansion-associated phenotypes. Cell Stem Cell. 2012; 11:264–278. [PubMed: 22748968]
44. La Spada AR, et al. Meiotic stability and genotype-phenotype correlation of the trinucleotide repeat in X-linked spinal and bulbar muscular atrophy. Nature genetics. 1992; 2:301–304. [PubMed: 1303283]
45. Nihei Y, et al. Enhanced aggregation of androgen receptor in induced pluripotent stem cell-derived neurons from spinal and bulbar muscular atrophy. The Journal of biological chemistry. 2013; 288:8043–8052. [PubMed: 23364790]
46. Ku S, et al. Friedreich's ataxia induced pluripotent stem cells model intergenerational GAATTC triplet repeat instability. Cell Stem Cell. 2010; 7:631–637. [PubMed: 21040903]
47. Sanchez-Danes A, et al. Disease-specific phenotypes in dopamine neurons from human iPS-based models of genetic and sporadic Parkinson's disease. EMBO Mol Med. 2012; 4:380–395. [PubMed: 22407749]
48. Burkhardt MF, et al. A cellular model for sporadic ALS using patient-derived induced pluripotent stem cells. Mol Cell Neurosci. 2013; 56C:355–364. [PubMed: 23891805]

Author Manuscript Author Manuscript Author Manuscript Author Manuscript

49. Yang YM, et al. A small molecule screen in stem-cell-derived motor neurons identifies a kinase inhibitor as a candidate therapeutic for ALS. Cell Stem Cell. 2013; 12:713–726. [PubMed: 23602540]

50. Brooks BP, et al. Characterization of an expanded glutamine repeat androgen receptor in a neuronal cell culture system. Neurobiol Dis. 1997; 3:313–323. [PubMed: 9173928]

51. Malik B, et al. Absence of disturbed axonal transport in spinal and bulbar muscular atrophy. Hum Mol Genet. 2011; 20:1776–1786. [PubMed: 21317158]

52. Marchetto MC, et al. A model for neural development and treatment of Rett syndrome using human induced pluripotent stem cells. Cell. 2010; 143:527–539. [PubMed: 21074045]

53. Bailey CK, Andriola IF, Kampinga HH, Merry DE. Molecular chaperones enhance the degradation of expanded polyglutamine repeat androgen receptor in a cellular model of spinal and bulbar muscular atrophy. Hum Mol Genet. 2002; 11:515–523. [PubMed: 11875046]

Author Manuscript Author Manuscript Author Manuscript Author Manuscript

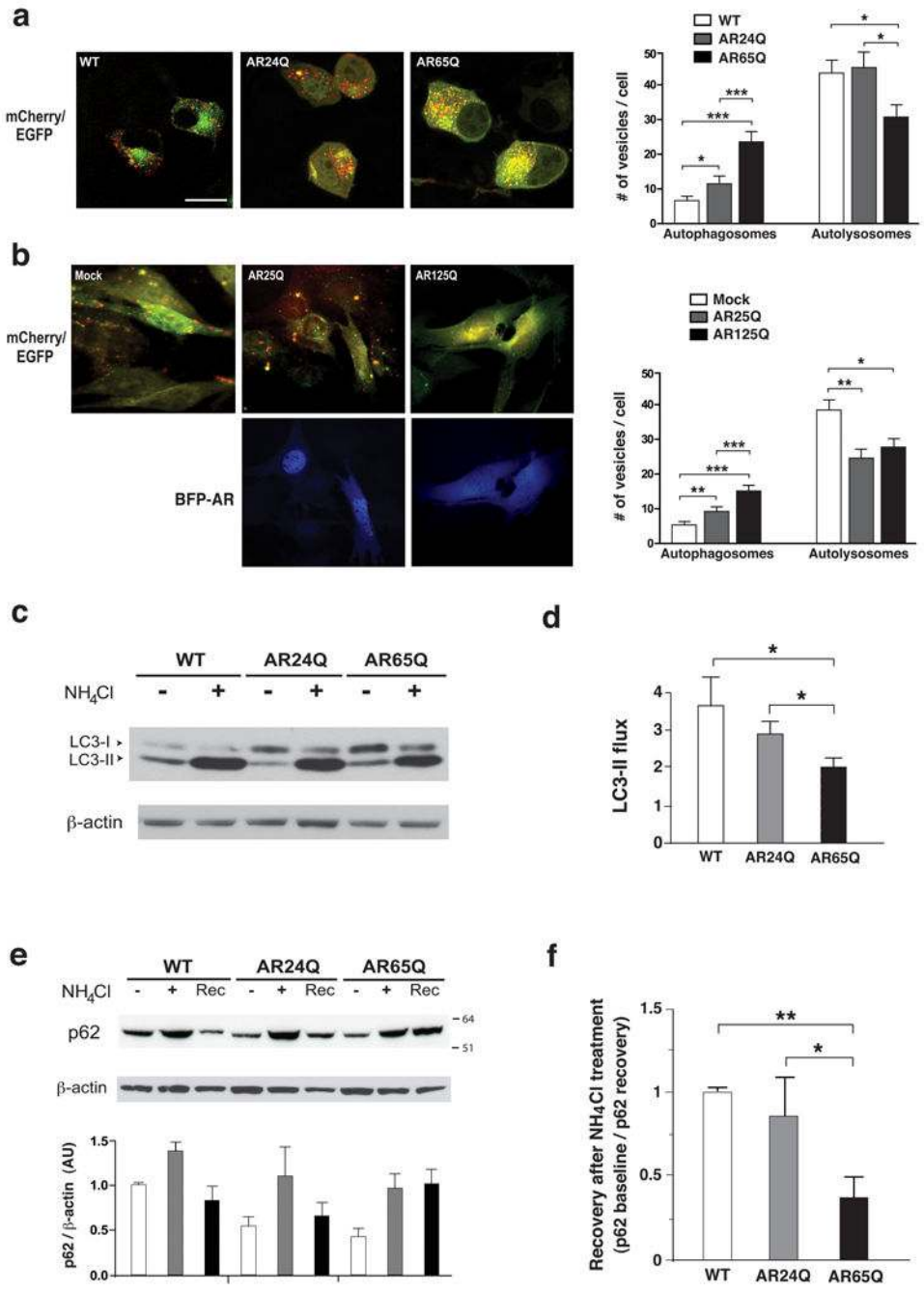

Figure 1. PolyQ-expanded AR retards autophagy pathway flux

(a) MN-1 cells were transfected with mCherry-EGFP-LC3 vector, fixed, and imaged after 24 hrs. Numbers of yellow puncta (autophagosomes) and red puncta (autolysosomes) per cell were counted. Autophagosomes: n = 3 independent experiments, F=3.56; autolysosomes: n = 3 independent experiments, F=20.13. One-way ANOVA with post-hoc Tukey test. **P* < .05, ***P* < .01, ****P* < .001. n = 34 cells / genotype.

(b) We transfected MEFs stably expressing mCherry-EGFP-LC3 with BFP-tagged AR25Q or AR125Q. Cells were imaged after 24 hrs, and yellow puncta (autophagosomes) and red

Author Manuscript Author Manuscript Author Manuscript Author Manuscript

puncta (autolysosomes) in AR-expressing (blue) cells were counted. Autophagosomes: n = 3 independent experiments, F=20.65; autolysosomes: n = 3 independent experiments, F=4.49. One-way ANOVA with post-hoc Tukey test. **P* < .05, ***P* < .01, ****P* < .001. n = 33 cells / genotype.

(c) MN-1 cells were immunoblotted for LC3 in the presence or absence of ammonium chloride to evaluate autophagic flux. A representative LC3 Western blot is shown. All ratios were normalized to MN-1 WT cells at baseline, which was set to 1.

(d) The ratio of LC3-II:actin was determined by densitometry analysis using ImageJ for **(c)**. n = 3 independent experiments, F=0.4501, one-way ANOVA with post-hoc Tukey test. **P* < .05.

(e) MN-1 cells were treated with ammonium chloride to block lysosomal activity, and then ammonium chloride was removed, and cells were allowed to degrade accumulated autophagy cargo during a 6 hr recovery period. We performed p62 Western blot analysis on MN-1 cells at baseline (-), after ammonium chloride treatment (+), and after the recovery period (Rec). All ratios were normalized to MN-1 WT cells at baseline, which was set to 1.

(f) Based upon the p62 values obtained in **(e)**, we calculated the efficiency of degraded accumulated autophagic cargo by dividing p62 at baseline by p62 at recovery, and normalized the baseline / recovery values to baseline / recovery for MN-1 WT cells, which was set to 1. n = 3 independent experiments, F=5.45, one-way ANOVA with post-hoc Tukey test. **P* < .05, ** *P* < .01.

Data are presented as mean ± s.e.m. Scale bar = 20 μm.

Author Manuscript Author Manuscript Author Manuscript Author Manuscript

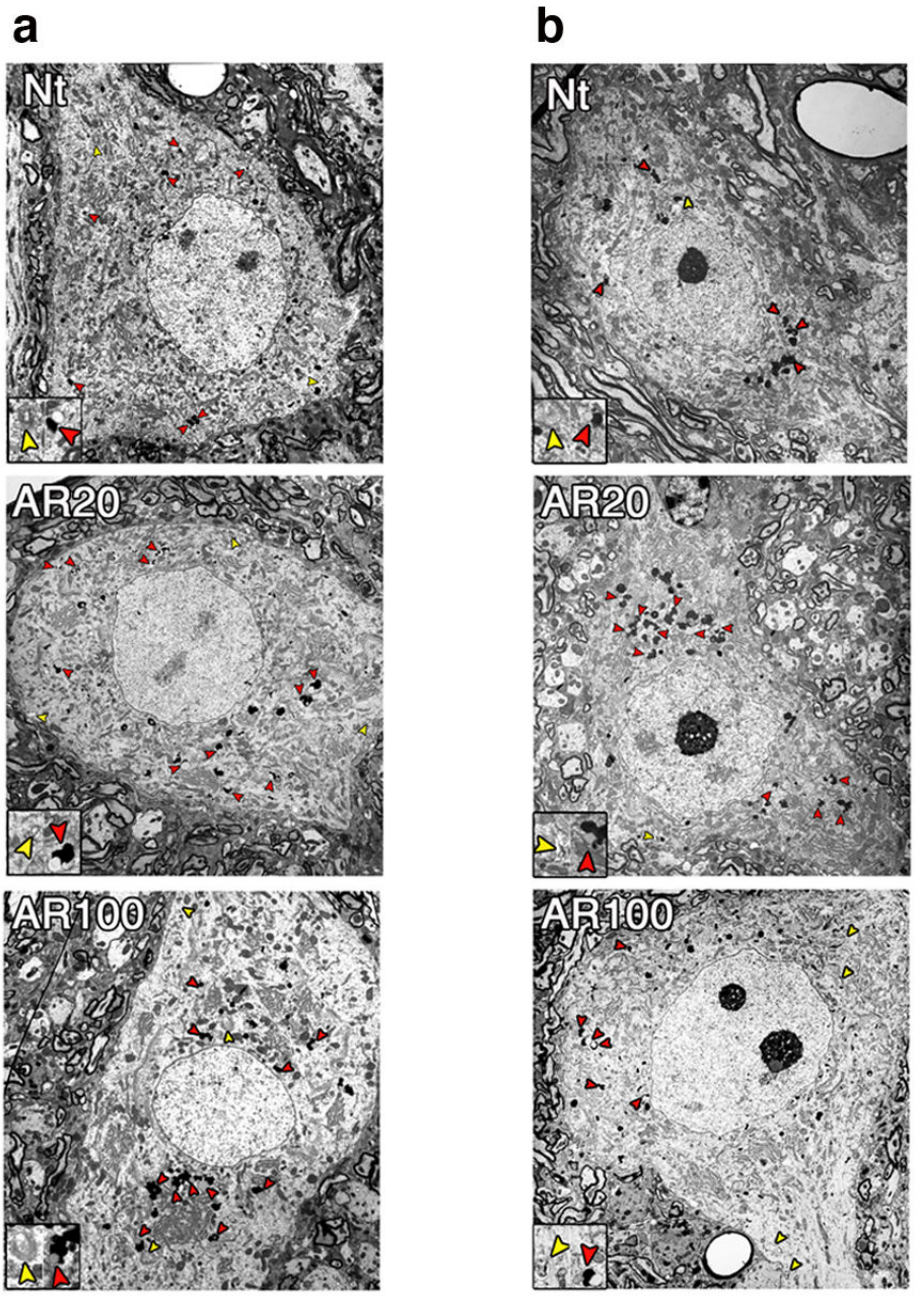

Figure 2. SBMA mice display accumulations of autophagosomes and reduced autolysosome formation in degenerating motor neurons

Electron micrographs of motor neuron perinuclear regions from age-matched non-transgenic (Nt), YAC AR20, and YAC AR100 transgenic mice prior to disease onset (**a,** 6 months of age), and after prominent neuromuscular and molecular pathology is apparent (**b,** 14 months of age).

(a) At 6 months of age, occasional autophagosomes (yellow arrowheads) are noted in Nt, YAC AR20, and YAC AR100 at roughly equivalent frequency. Autolysosomes (red arrowheads) are much more common, and are present in higher numbers in YAC AR20 and YAC AR100 motor neurons.

Author Manuscript Author Manuscript Author Manuscript Author Manuscript

(b) At 14 months of age, when YAC AR100 mice display signs of motor neuronopathy and molecular pathology, we observed many YAC AR100 motor neuron micrographs with frequent autophagosomes (yellow arrowheads). Despite this increase in autophagosomes, autolysosomes were fewer in number at this age in YAC AR100 motor neurons, such that autophagosome numbers approached that of autolysosome numbers in YAC AR100 motor neurons. This was never the case for Nt motor neurons or YAC AR20 motor neurons. Main panels are at 2200× magnification and insets are at 3700× magnification.

Author Manuscript Author Manuscript Author Manuscript Author Manuscript

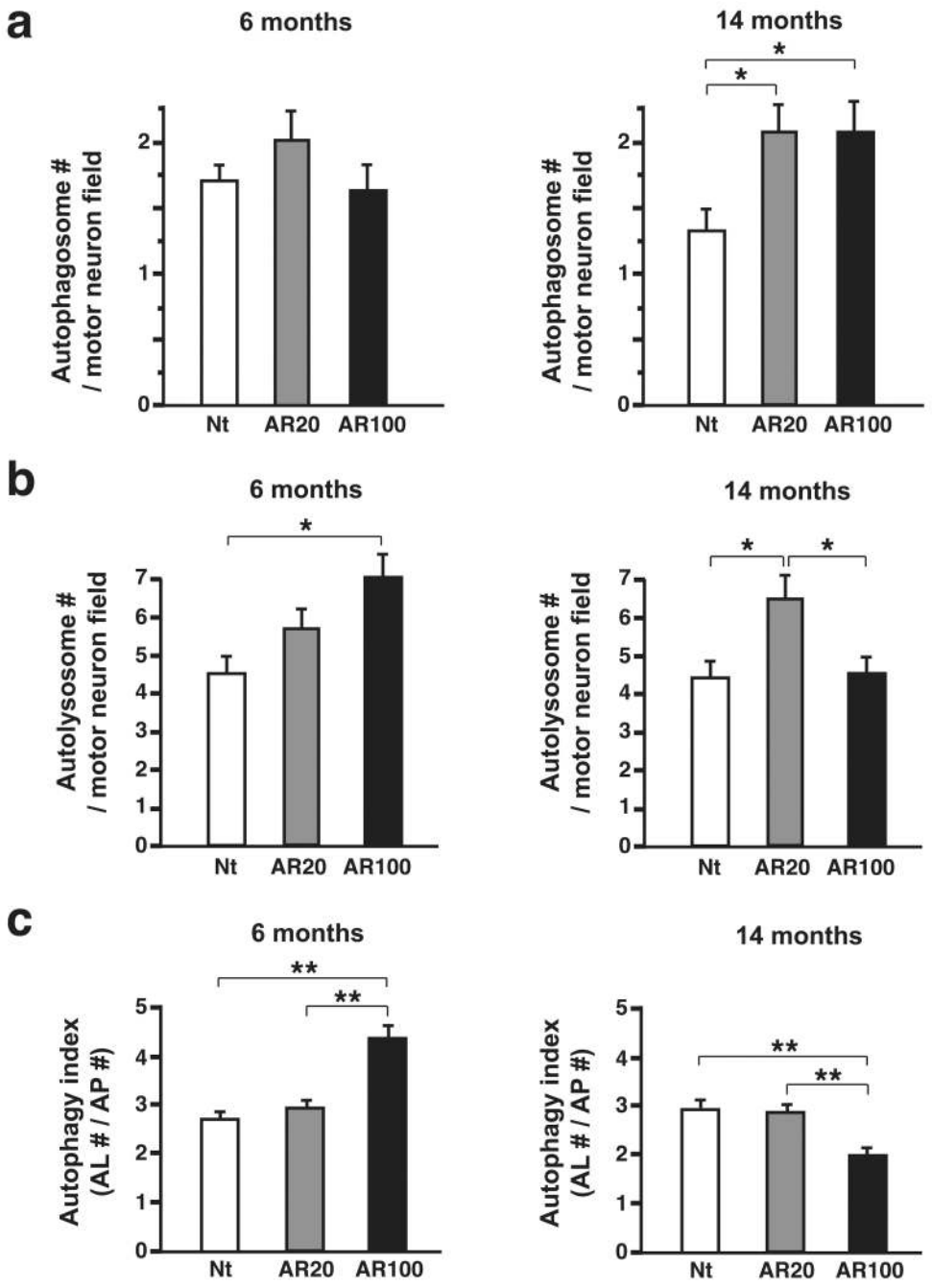

Figure 3. Quantification of autophagic vesicle type uncovers impaired autophagy progression

(a) We counted the number of autophagosomes (APs) / motor neuron field in electron micrographs from non-transgenic (Nt), YAC AR20, and YAC AR100 transgenic mice at 6 and 14 months of age. Data are presented as mean AP numbers / motor neuron field ± s.e.m. 6 months: n = 3 independent experiments, F=0.63, one-way ANOVA with post-hoc Tukey test. *P* = .534. 14 months: n = 3 independent experiments, F=4.32, one-way ANOVA with post-hoc Tukey test. **P* < .05.

Author Manuscript Author Manuscript Author Manuscript Author Manuscript

(b) We counted the number of autolysosomes (ALs) / motor neuron field in electron micrographs form Nt, YAC AR20, and YAC AR100 transgenic mice at 6 and 14 months of age. Data are presented as mean AL numbers / motor neuron field ± s.e.m. 6 months: n = 3 independent experiments, F=4.18, one-way ANOVA with post-hoc Tukey test. *$P < .05$. 14 months: n = 3 independent experiments, F=4.56, one-way ANOVA with post-hoc Tukey test. *$P < .05$.

(c) We calculated an autophagy index by dividing AL number by AP number for each motor neuron field. Data are presented as mean autophagy index ± s.e.m. At 6 months, YAC AR100 motor neurons displayed a markedly increased autophagy index; n = 3 independent experiments, F=129.81, one-way ANOVA with post-hoc Tukey test. **$P < .01$. However, once YAC AR100 mice develop disease pathology at 14 months, the autophagy index for YAC AR100 motor neurons is significantly decreased; n = 3 independent experiments, F=82.82, one-way ANOVA with post-hoc Tukey test. **$P < .01$.

Author Manuscript Author Manuscript Author Manuscript Author Manuscript

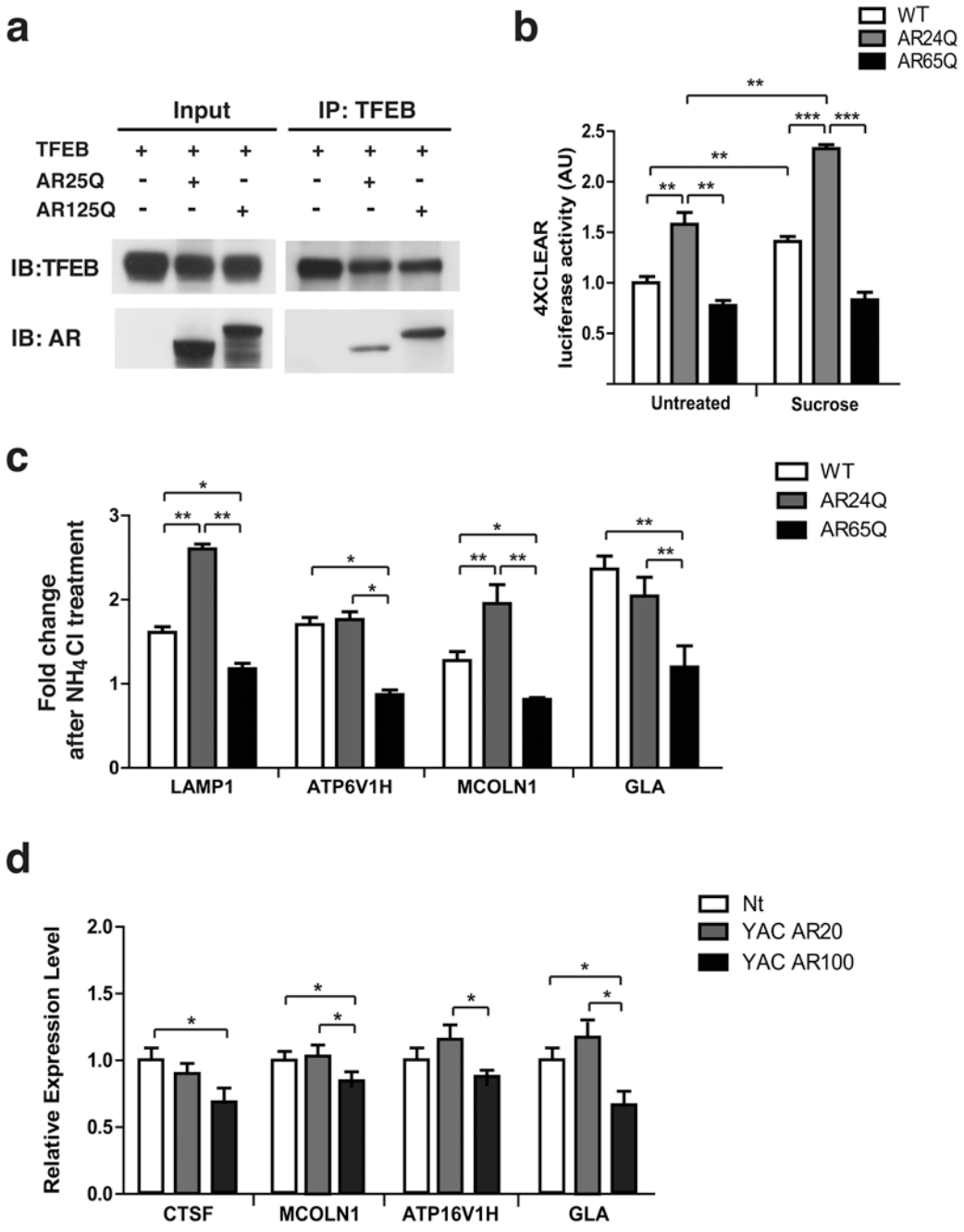

Figure 4. PolyQ-expanded AR interferes with TFEB transactivation function

(a) HEK293 cells were co-transfected with TFEB and AR25Q or AR125Q, as indicated. Immunoprecipitation was performed with anti-TFEB antibody, followed by immunoblotting for TFEB and AR. Untransfected HEK293 cells served as a negative control, and no AR was observed with IgG antibody only (not shown).

(b) We transfected MN-1 cells with the 4X-CLEAR luciferase reporter, and treated cells with sucrose to induce TFEB activation. Baseline: n = 3 independent experiments, F=3.48, one-way ANOVA with post-hoc Tukey test. $^{**}P < .01$. Sucrose treatment: n = 3

Author Manuscript Author Manuscript Author Manuscript Author Manuscript

independent experiments, **P < .01, t-test, WT t(10)=8.133; ***P < .001, t-test, AR 24Q t(10)=6.11; P = n.s., AR 65Q t(10)=0.644. Sucrose-treated MN-1 AR24Q cells displayed significantly higher 4X-CLEAR luciferase activity; n = 3 independent experiments, F=2.49, one-way ANOVA with post-hoc Tukey test. ***P < .001.

(c) We exposed MN-1 cells to ammonium chloride, an inhibitor of lysosomal activity, to determine the capacity for TFEB induction. RT-PCR analysis revealed lack of TFEB target gene induction in MN-1 AR65Q cells for four gene targets: *LAMP1* (lysosomal-associated membrane protein 1) [F=37.51]; *ATP16V1H* (vesicular ATPase subunit 16) [F=57.26]; *MLCOLN1* (mucolipin1) [F=251.0]; and *GLA* (galactosidase-α) [F=75.51]; n = 3 independent experiments, *P < .05, **P < .01, ANOVA with post-hoc Tukey test. For *LAMP1* and *MLCOLN1*, MN-1 AR24Q cells yielded significantly higher expression. Differences in the expression of TFEB target genes at baseline were negligible.

(d) We measured expression levels of TFEB target genes in embryonic day 13 (E13) motor neurons derived from non-transgenic (Nt), YAC AR20, and YAC AR100 mice by RT-PCR analysis: *CTSF* (cathepsin F) [F = 4.63]; *MLCOLN1* (mucolipin1) [F=6.64]; *ATP16V1H* (vesicular ATPase subunit 16) [F = 5.6]; and *GLA* (galactosidase-α) [F = 5.65]; n = 3 independent experiments, *P < .05, ANOVA with post-hoc Tukey test. Data are presented as mean ± s.e.m.

Author Manuscript Author Manuscript Author Manuscript Author Manuscript

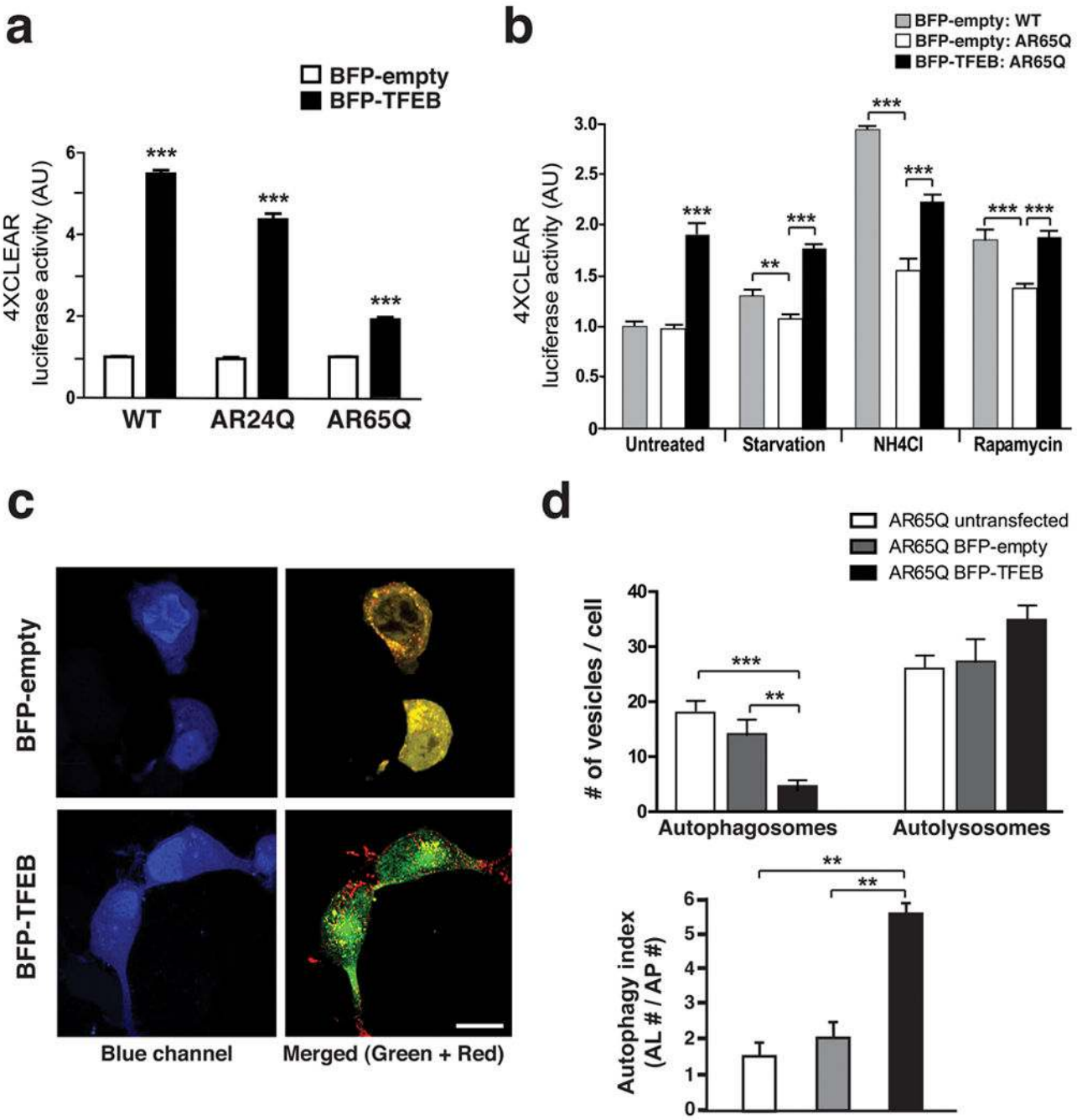

Figure 5. TFEB over-expression rescues impaired 4X-CLEAR transactivation and retarded autophagic flux in MN-1 AR65Q cells

(a) We transfected MN-1 cells with the 4X-CLEAR luciferase reporter, and with BFP-tagged TFEB or BFP empty vector, and then measured luciferase activity. Marked induction of luciferase activity occurred with BFP-TFEB; n = 3 independent experiments, ***P < .001, t-test, WT t(4)=48.79; ***P < .001, t-test, AR 24Q t(4)=22.91; ***P < .001, t-test, AR 65Q t(4)=14.02. Results for each line were normalized to the BFP-empty luciferase activity, which was set to 1.

Author Manuscript Author Manuscript Author Manuscript Author Manuscript

(b) We transfected MN-1 AR65Q cells with the 4X-CLEAR luciferase reporter, and with BFP-TFEB or BFP empty vector, and subjected the MN-1 AR65Q cells to conditions that promote TFEB activation, as shown. MN-1 WT cells were also transfected with the 4X-CLEAR luciferase reporter and BFP empty vector, and subjected to the identical treatments for control purposes. Results are shown normalized to untreated MN-1 WT cells expressing BFP-empty, which was set to 1; Untreated, F=182.7; STV, F=63.64; NH4Cl, F=291.9; Rapamycin, F=3128; ANOVA with post-hoc Tukey test. $^{**}P < .01$, $^{***}P < .001$.
(c) We transfected MN-1 AR65Q cells with the mCherry-EGFP-LC3 construct and with either BFP-empty or BFP-TFEB. Autophagic vesicles forming in BFP-expressing cells were then detected as red, green, or yellow puncta, as shown. Scale bar = 20 μm.
(d) Quantification of autophagic vesicle type. Note marked reduction in autophagosomes in MN-1 AR65Q cells expressing BFP-TFEB; n = 3 independent experiments, F=16.596, ANOVA with post-hoc Tukey test. $^{*}P < .05$. Calculation of the autophagy index; n = 3 independent experiments, F=24.43, ANOVA with post-hoc Tukey test. $^{**}P < .01$. Data are presented as mean ± s.e.m.

Author Manuscript Author Manuscript Author Manuscript Author Manuscript

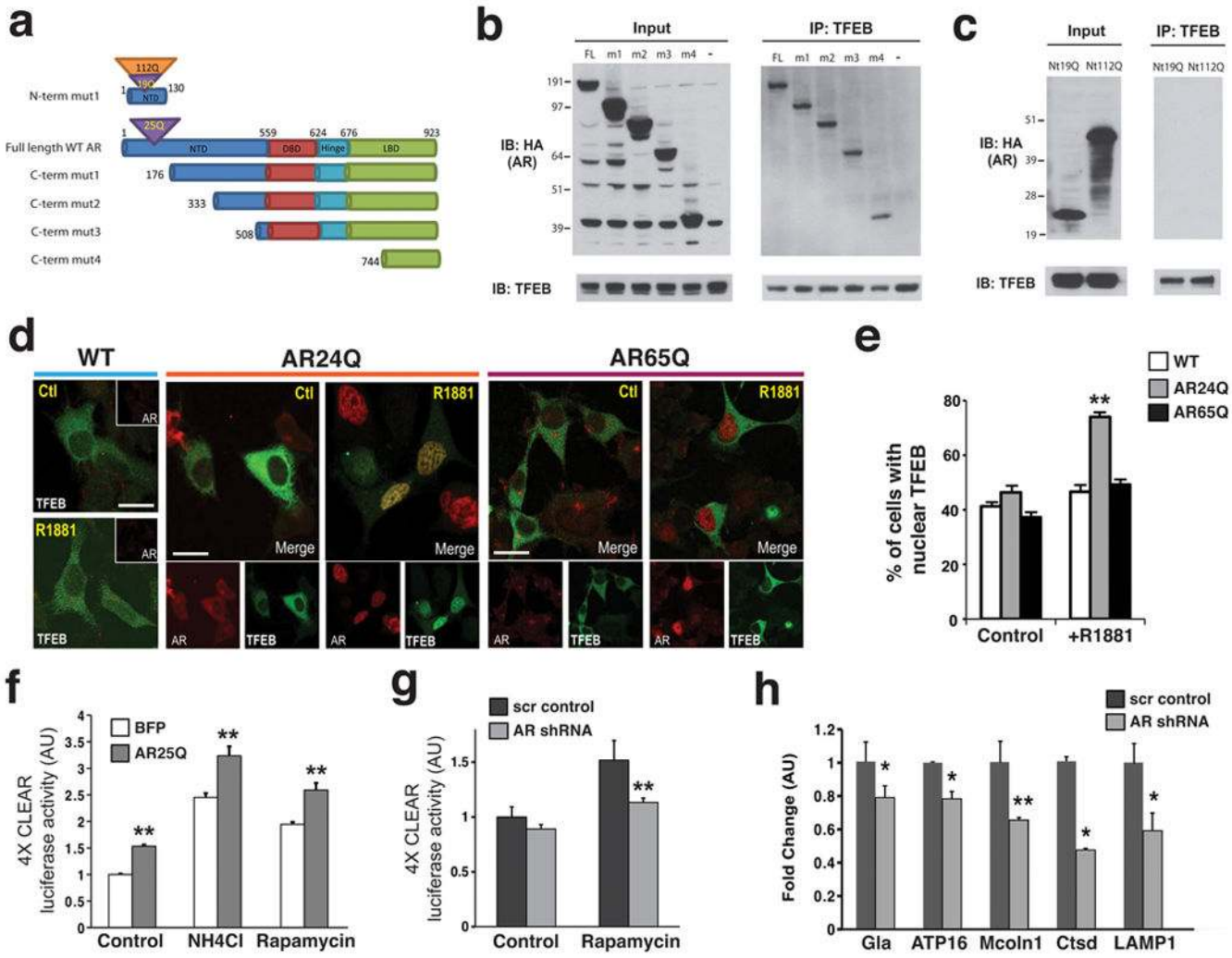

Figure 6. AR interacts with and co-activates TFEB

(a) Diagram of AR truncation constructs. NTD, N-terminal domain; DBD, DNA binding domain; Hinge, Hinge domain; LBD, ligand binding domain

(b) HEK293 cells were co-transfected with TFEB and HA-tagged full-length AR25 (FL) or a C-terminal AR mutant (m1, m2, m3, m4). Immunoprecipitation was performed with anti-TFEB antibody, followed by immunoblotting for TFEB and AR. Untransfected HEK293 cells served as a negative control, and no AR was observed with IgG antibody only (not shown).

(c) HEK293 cells were co-transfected with TFEB and HA-tagged N-terminal AR mutant containing a 19Q or 112Q tract (Nt19Q, Nt112Q). Immunoprecipitation was performed as in **(b)**.

(d) MN-1 WT, MN-1 AR24Q, and MN-1 AR65Q cells were cultured in standard media or in media supplemented with R1881, and then immunostained with anti-AR and anti-TFEB antibodies. Cells were scored for nuclear or cytosolic localization of TFEB. Scale bar = 20 μm.

Author Manuscript Author Manuscript Author Manuscript Author Manuscript

(e) Quantification of **(d)**. F=0.56 [untreated], F=5.51 [R1881-treated], ANOVA with post-hoc Tukey test. ***P* < .01.

(f) We transfected MN-1 WT cells with the 4X-CLEAR luciferase reporter and either BFP-empty or AR25Q-BFP, under standard culture conditions (Control), ammonium chloride treatment, or rapamycin treatment. t(3)=15.73 [Control], t(4)=4.108 [NH4Cl], t(4)=4.58 [rapamycin], t-test. ***P* < .01.

(g) We transfected MN-1 AR24Q cells with either scrambled shRNA control vector or AR shRNA vector, and measured 4X-CLEAR luciferase reporter activity under baseline conditions (Control) or after rapamycin. t(4)=0.51 [Control], t(4)=7.15 [rapamycin], t-test. ***P* < .01.

(h) RT-PCR analysis of MN-1 AR24Q cells transfected with scrambled shRNA control or AR shRNA vector: *GLA* (galactosidase-α) [t(4)=4.77], *ATP16* (vesicular ATPase subunit 16) [t(4)=3.75]; *MLCOLN1* (mucolipin1) [t(4)= 13.74]; *CTSD* (Cathepsin D) [t(4)=7.91], and *LAMP1* (lysosomal-associated membrane protein 1) [t(4)=6.46]; n = 3 independent experiments, **P* < .05, ***P* < .01, t-test. Data are presented as mean ± s.e.m.

Author Manuscript Author Manuscript Author Manuscript Author Manuscript

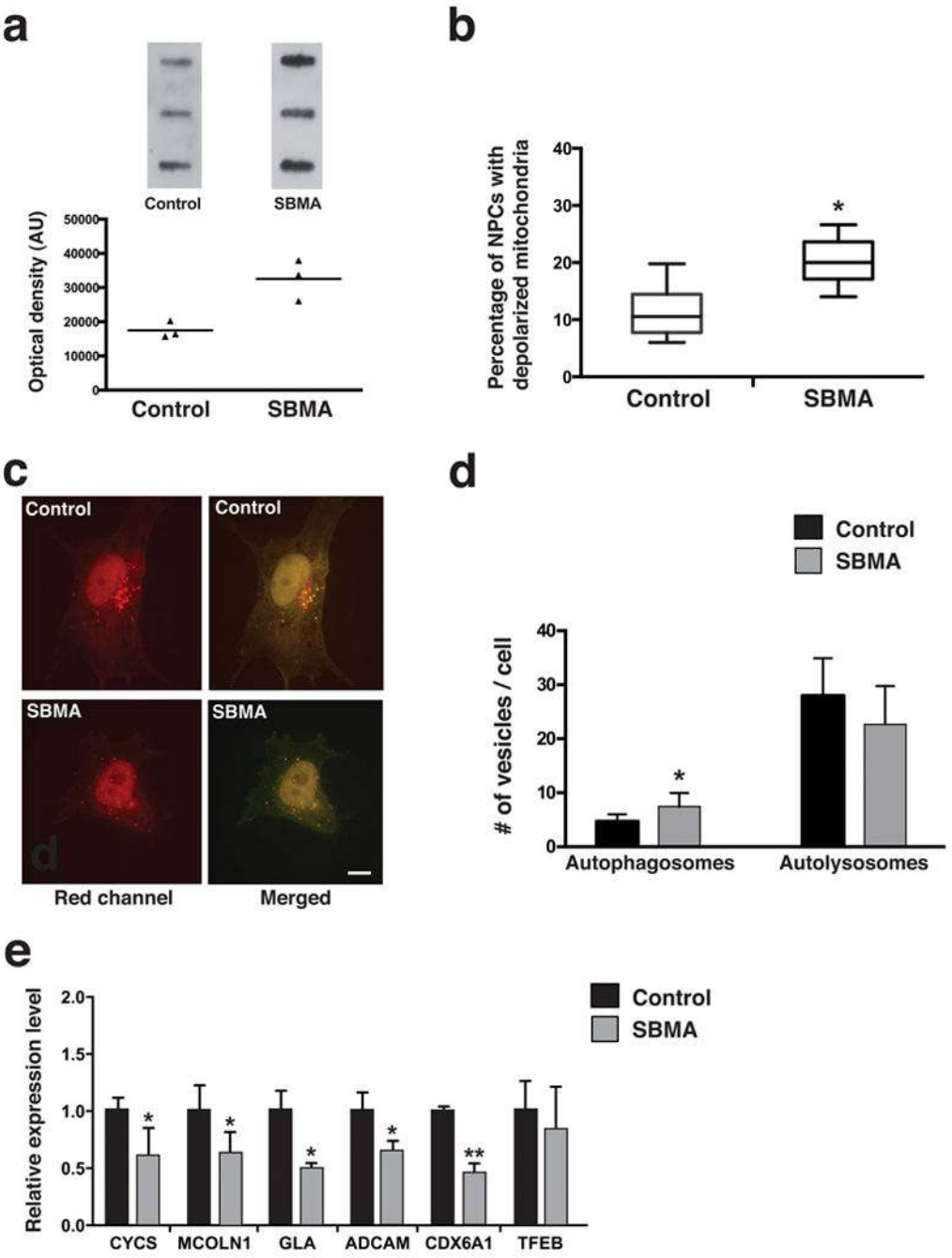

Figure 7. SBMA-derived neuronal precursor cells exhibit mitochondrial depolarization and autophagy flux phenotypes

(a) We performed filter-trap assays to determine the extent of accumulation of insoluble AR protein in NPC lines from three different controls and three different SBMA patients. Significantly higher levels of insoluble AR protein were present in the SBMA NPC lines, based upon densitometry analysis; n = 3 independent experiments, **P* < .05, t-test, t(4)=4.026.

Author Manuscript Author Manuscript Author Manuscript Author Manuscript

(b) NPCs from three different controls and three different SBMA patients were cultured in the presence of JC-1 dye. Results are presented as a Tukey box-plot with 1.5 interquartile range; n = 3 independent experiments, **P* < .05, t-test, t(4)=3.983.
(c) We transfected NPC lines derived from SBMA patients and controls (three different NPC lines / human case) with the mCherry-EGFP-LC3 vector. Autophagic vesicles were detected as colored puncta, as shown. Scale bar = 10 μm.
(d) Quantification of autophagic vesicle type from **(c)**. SBMA NPCs exhibit a significant increase in autophagosomes; n = 18 different samples: 3 clones/line, 3 lines/group, **P* < .05, t-test; t(18)=2.3799 [APs].
(e) We isolated RNAs from SBMA and control NPC lines (three different NPC lines / human case), and then measured the expression levels of TFEB target genes including: *CYCS* (cytochrome c), t(4)=2.844; *MLCOLN1* (mucolipin1), t(4)=3.246; *GLA* (galactosidase-α), t(4)=3.174; *ACADM* (Acyl-CoA dehydrogenase), t(4)=4.405; *COX6A1* (cytochrome oxidase 6A1), t(4)=5.584; and the TFEB gene itself, t(4)=0.593. Significant expression reductions were noted in SBMA NPC lines for all tested TFEB target genes. **P* < .05, ***P* < .01. Data are presented as mean ± s.e.m.

Author Manuscript Author Manuscript Author Manuscript Author Manuscript

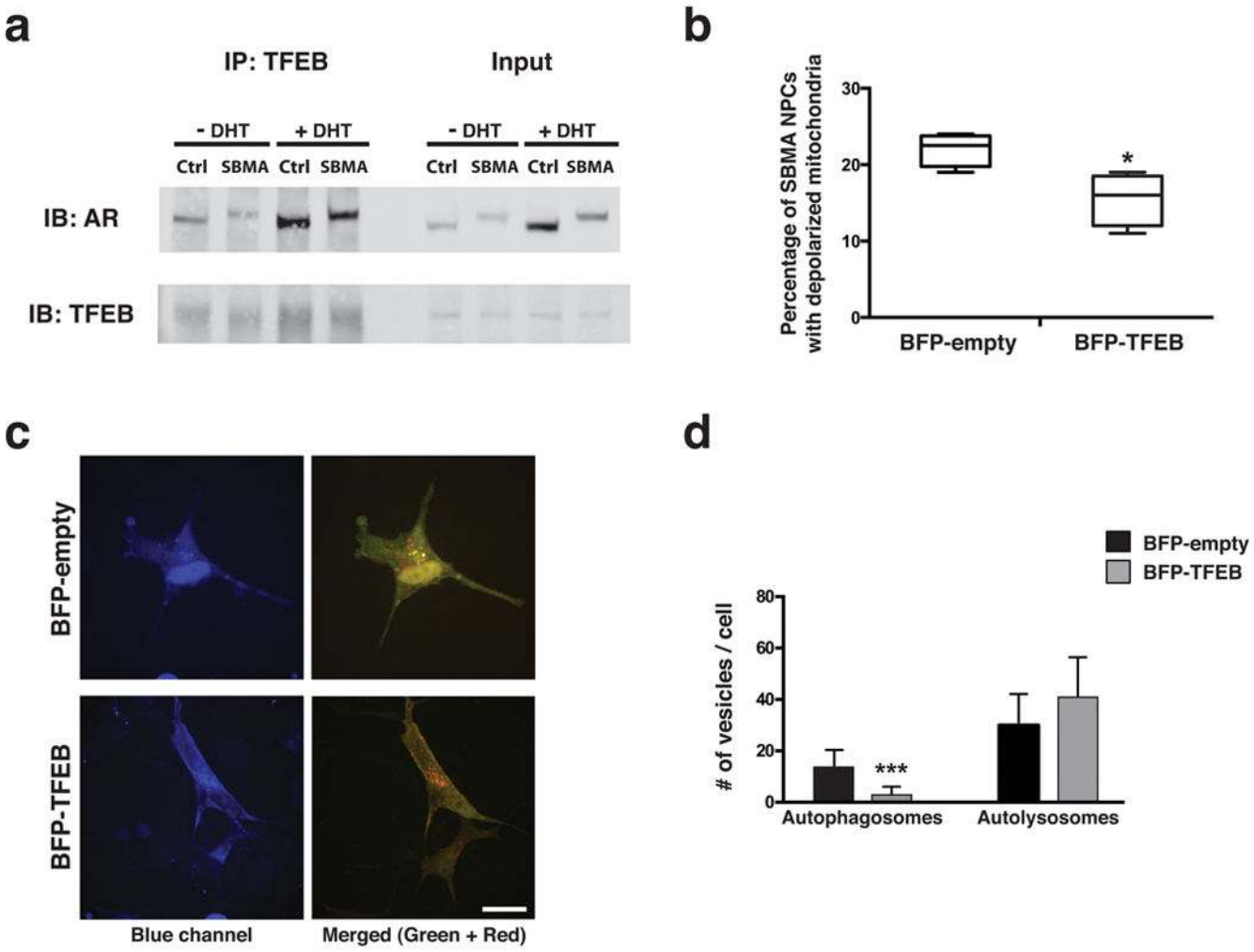

Figure 8. TFEB rescues metabolic and autophagic flux defects in SBMA NPCs

(a) Control and SBMA NPC lines were maintained in the presence or absence of the AR ligand dihydrotestosterone (DHT) and then harvested for immunoblotting analysis after TFEB antibody immunoprecipitation. Immunoblotting for AR confirmed expression of AR in control (Ctrl) and SBMA NPCs, and immunoblotting for TFEB confirmed the interaction of AR with TFEB in both control and SBMA NPCs.

(b) We transfected SBMA NPC lines (three different NPC lines / patient) with either the BFP-empty vector or BFP-TFEB expression construct, treated the NPCs with JC-1 dye, and counted the percentage of cells with depolarized mitochondria. Results are presented as a Tukey box-plot with 1.5 interquartile range; n = 3 independent experiments, $*P < .05$, t-test, t(6)=3.217.

(c) Here we see representative images from transfection of SBMA NPCs with the mCherry-EGFP-LC3 vector and either BFP-empty vector or BFP-TFEB expression construct. BFP-empty vector expressing SBMA NPCs display a preponderance of yellow puncta (autophagosomes), while BFP-TFEB expressing SBMA NPCs exhibit a shift towards almost entirely red puncta (autolysosomes), consistent with rescue of the autophagic flux defect. Scale bar = 20 μM.

Author Manuscript Author Manuscript Author Manuscript Author Manuscript

(d) We transfected SBMA NPC lines (three different NPC lines / patient) with the mCherry-EGFP-LC3 vector and either BFP-empty vector or BFP-TFEB expression construct, counted the number of autophagosomes and autolyosomes in BFP-expressing NPCs, and determined the number of autophagic vesicles per cell. TFEB over-expression markedly reduced autophagosome formation in SBMA NPCs; ***$P < .001$; t-test, t(30)=4.373. Data are presented as mean ± s.e.m.